iScience

CellPress

Article

Enzyme Mimicking Based on the Natural Melanin Particles from Human Hair

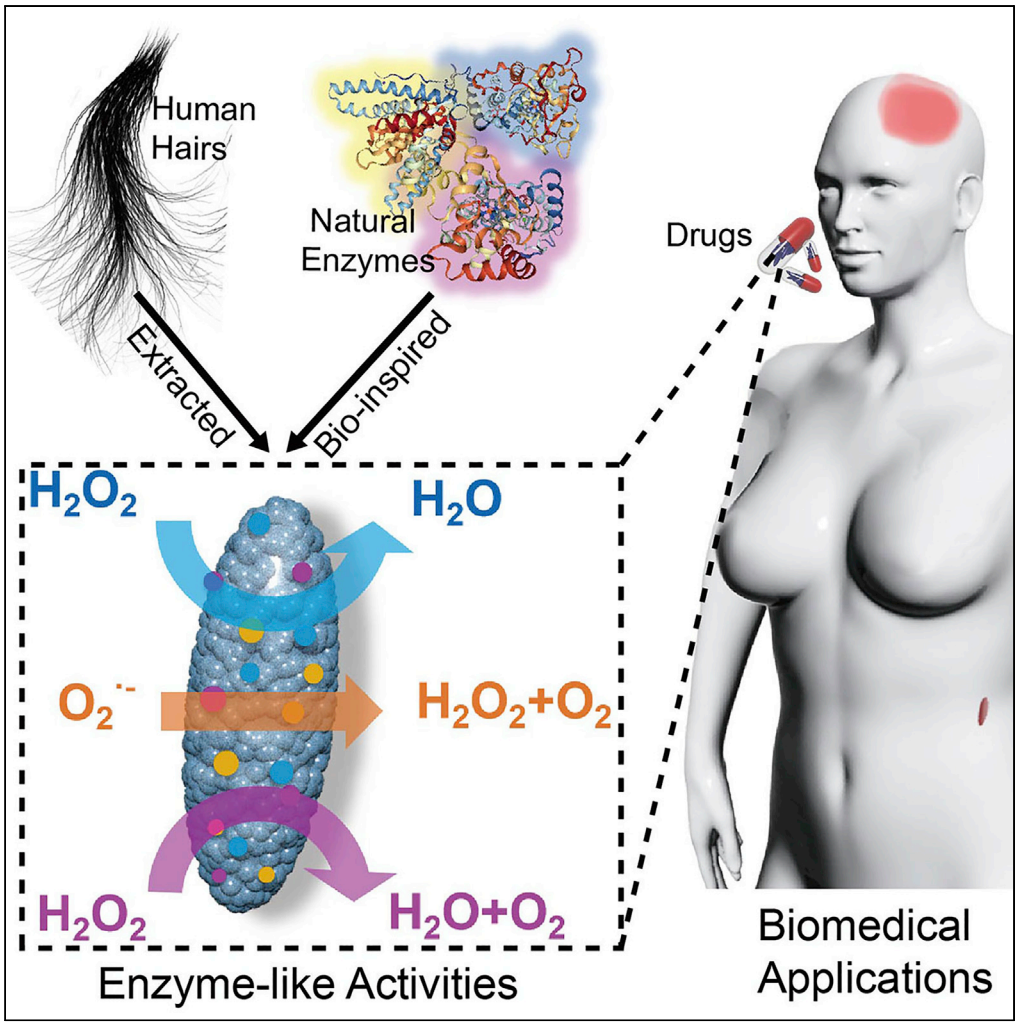

Sheng Hong, Qiu-Ling Zhang, Di-Wei Zheng, ..., Jing-Jie Ye, Han Cheng, Xian-Zheng Zhang

xz-zhang@whu.edu.cn

HIGHLIGHTS

Natural enzyme mimicking based on human hairs

Efficient, stable, and low-cost enzyme alternatives

Different enzyme-like activities of different M-NMPs

Enzyme-like activities provide the potential in biomedical application

Hong et al., iScience *23*, 100778
January 24, 2020
https://doi.org/10.1016/j.isci.2019.100778

iScience

CellPress

Article

Enzyme Mimicking Based on the Natural Melanin Particles from Human Hair

Sheng Hong,[1] Qiu-Ling Zhang,[1] Di-Wei Zheng,[1] Cheng Zhang,[1] Yu Zhang,[1] Jing-Jie Ye,[1] Han Cheng,[1] and Xian-Zheng Zhang[1,2,*]

SUMMARY

Natural enzymes are mainly composed by the protein part and metallic cofactor part, both of which work cooperatively to achieve high catalytic activity. Here, natural melanin particles (NMPs) were extracted from human hair and further bound with metal ions to mimic natural enzymes. The different metal-bound NMPs (M-NMPs) exhibited different enzyme-like activities with great promise in diverse biomedical applications. It was found that Fe-bound NMPs (Fe-NMPs) showed outstanding peroxidase (POD)-like activity that possessed potential in antibacterial applications, and Mn-bound NMPs (Mn-NMPs) displayed catalase (CAT)-like activity with a remarkable radiotherapy sensitization effect in cancer therapy. Besides, Cu-bound NMPs (Cu-NMPs) could serve as combined POD, superoxide dismutase (SOD), and CAT alternatives, which exhibited prominent reactive oxygen species (ROS) scavenging ability, revealing great potential in anti-inflammation. The versatile enzyme-like activities of M-NMPs derived from hair might give extensive perspective for designing biomedical materials and provide a promising tool in solving biomedical problems.

INTRODUCTION

Natural enzymes, playing crucial roles in all the life activities, have been extensively applied in various fields owing to their superior performance (Chen et al., 2018; Li et al., 2017; Triplett et al., 2018; Wu et al., 2019; Yang et al., 2018). However, intrinsic drawbacks of natural enzymes such as high cost and low stability seriously limit their practical applications. To overcome the disadvantages, great efforts have been made to develop natural enzyme alternatives with high performance (Wei and Wang, 2013; Yang et al., 2019). In the past few decades, varieties of bio-inspired nanomaterials have been proposed to harbor enzyme-like activities for serving as high-performance natural enzyme alternatives (Wang et al., 2016, 2018). For example, MnO_2 and CeO_2 nanoparticles have been reported to possess both catalase (CAT)-like and superoxide dismutase (SOD)-like catalytic activities that can protect cells against oxidative damages through eliminating harmful reactive oxygen species (ROS) (Kim et al., 2012; Li et al., 2017). In addition, Fe_3O_4 nanoparticles also exhibited peroxidase (POD)-like activity for immunohistochemical detection (Fan et al., 2012; Gao et al., 2007). Although these enzyme alternatives showed considerable potential applications in biomedicine, the low efficiency and unsatisfied selectivity still restrict their practical applications.

In general, natural enzymes are mainly consisting of the protein part and metallic cofactor part. The protein part, namely the peptide chain containing functional groups such as amino, carboxyl, hydroxy, and indolyl groups, could adsorb the substrate and provide active sites for the convenience of substrate binding. And the metallic cofactor part is generally metal ion or the metal complex, playing an important role in electron transmission. Both of them are indispensable for working together to achieve the catalytic activity of enzymes (Zastrow et al., 2011; Lu et al., 2009). For example, POD, a kind of protein containing iron porphyrin as cofactor, could catalyze the oxidation of substrate by hydrogen peroxide as electron acceptor (Das and Hecht, 2007). Cu and Mn were also found to act as the active center in SOD, an enzyme disproportionation of superoxide anion, which could serve as a significant antioxidant enzyme in nearly all living cells (Robinson and Winge, 2010; Huang et al., 2000).

It is well known that melanin in human hair exists in the form of melanin granules, which was reported to contain plenty of functional groups such as amino, carboxyl, and indolyl groups (Cho et al., 2017;Mostert et al., 2018; D'Ischia et al., 2014). In our previous study, natural melanin particles (NMPs) were extracted from human hair by using alkaline-degradation method, also confirming the presence of functional groups (Zheng et al., 2018). Here, NMPs, extracted from human hairs, were bound with metal ions to mimic the natural enzymes (Scheme 1). On the one hand, the abundant functional groups in NMPs could adsorb

[1]Key Laboratory of Biomedical Polymers of Ministry of Education & Department of Chemistry, Wuhan University, Wuhan 430072, P. R. China

[2]Lead Contact

*Correspondence: xz-zhang@whu.edu.cn

https://doi.org/10.1016/j.isci.2019.100778

Scheme 1. Schematic Illustration Showing the Fabrication and Multi-Enzyme Activity of Metal-Bound Natural Melanin Particles (NMPs) for Various Biomedical Applications

Inspired by natural enzymes, NMPs are extracted from human hair by alkali-heat-treatment and further bound with metal ions to mimic natural enzyme activity.

substrate and provide active sites for substrate binding as the protein part in natural enzymes. On the other hand, the metal ions in NMPs could also work as the metallic cofactor of enzyme (Scheme 1). It is hoped that the metal-bound NMPs (M-NMPs) derived from human hairs could serve as efficient, stable, and low-cost enzyme alternatives, providing a new view and useful tool for future biomedical applications.

RESULTS AND DISCUSSION

Preparation and Characterization of M-NMPs

The morphology and size of NMPs were characterized by transmission electron microscope (TEM), scanning electron microscope (SEM), and atomic force microscope (AFM). As presented in Figures 1A–1C, NMPs showed uniform fusiform shapes with an average length of 1.2 μm and width of 0.3 μm. Here, the Fe, Cu, and Mn ions were bound into the NMPs, and the enzyme-like activities of different M-NMPs were studied. The mapping images in Figure 1D showed a uniform distribution of C, O, N, and metal elements over the entire structure of its corresponding M-NMPs, indicating the successful binding of metal ions into NMPs. Furthermore, the energy dispersive spectrums (EDS) of M-NMPs also proved the successful binding of metal ions (Figure 1E). And the Fe, Cu, and Mn content in its corresponding M-NMPs analyzed by inductively coupled plasma mass spectrometry (ICP-MS) were 4.0wt%, 5.1wt%, and 4.2wt%, respectively (Table S1). Besides, the stability of M-NMPs was analyzed by measuring the change of mean size and the metal content, which were found to have no obvious change (Figure S1).

Enzyme-like Activities of M-NMPs

After successfully fabricating the M-NMPs, the enzyme-like activities were analyzed. First, the POD-like activity was evaluated by the oxidation of 3, 3′, 5, and 5′-tetramethylbenzidine (TMB). In the presence of H_2O_2, the colourlessTMB could be oxidized by POD to generate blue oxidized TMB (oxTMB) accompanied by an obvious increasing absorption at 650 nm (Fan et al., 2018). According to Figure 2A, the markedly increased absorption at 650 nm was observed only in the presence of Fe-NMPs and Cu-NMPs, suggesting their remarkable POD-like activity. And the color change from colourlessTMB to blue oxTMB also

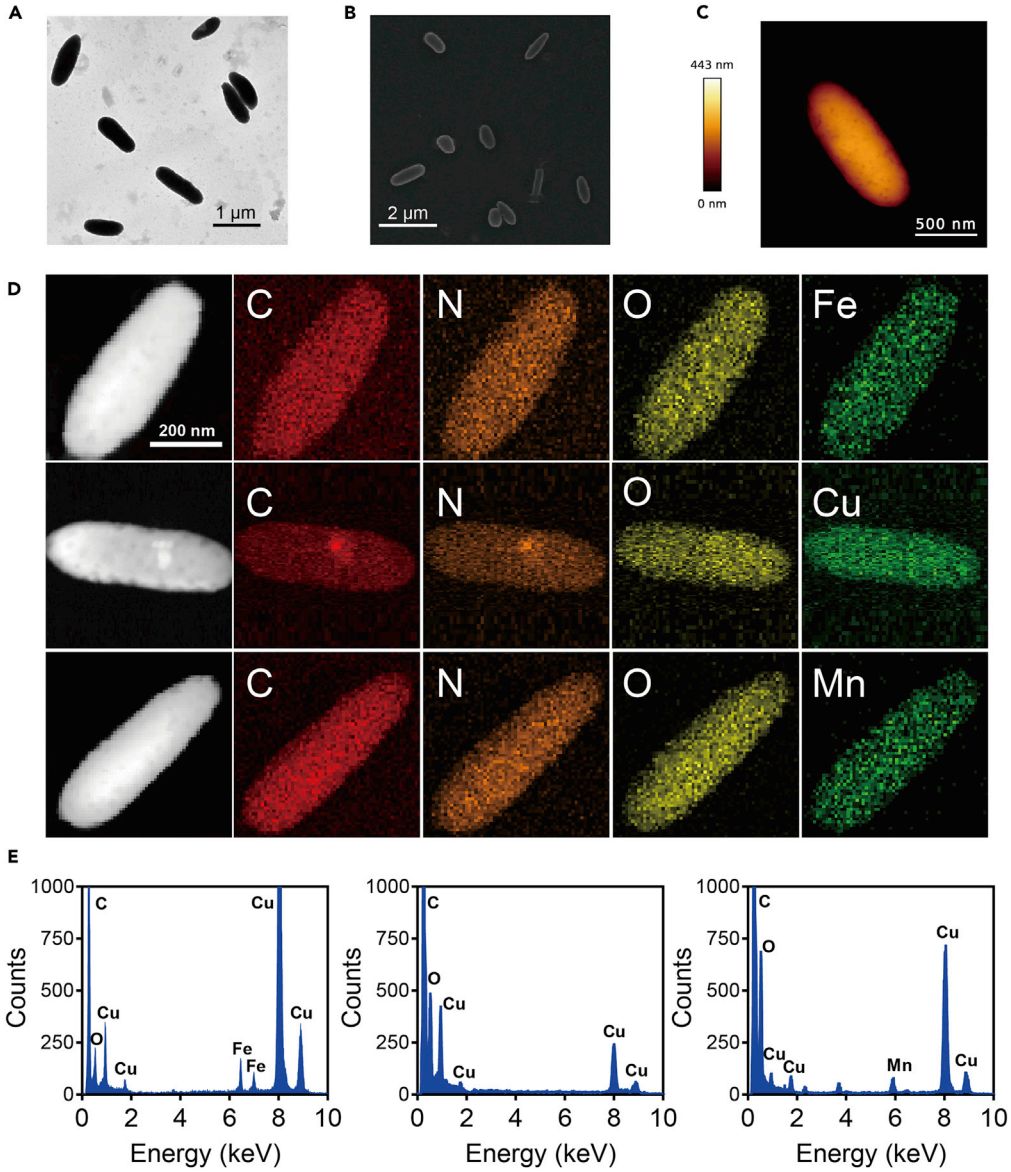

Figure 1. Characterization of NMPs and M-NMPs

(A–C) TEM (A), SEM (B), and AFM (C) images of NMPs obtained from human hair.

(D) Corresponding TEM elemental mappings of Fe-NMPs, Cu-NMPs, and Mn-NMPs.

(E) Energy dispersive spectrums (EDS) of Fe-NMPs, Cu-NMPs, and Mn-NMPs.

See also Figure S1 and Table S1.

confirmed the same result. The effect of catalyst concentration on its activity was further investigated. It was found that the absorbance in 650 nm increased gradually with the concentration of catalysts increasing (Figures 2B, 2C, and S2). The stability of catalysts was also studied in different pH and temperature conditions. Figure S3 demonstrated that Fe-NMPs and Cu-NMPs could retain high catalytic efficiency over a wide range of pH and temperature. Here, the Michaelis-Menten equation in enzyme kinetics was introduced to intuitively assess the catalytic activity of Fe-NMPs and Cu-NMPs. The calculated Michaelis constant of the two catalysts for H_2O_2 and TMB indicated their comparable affinity to the substrates (Figure S4 and Table S2), demonstrating that Fe-NMPs and Cu-NMPs exhibited markedly POD-like activity.

The SOD-like activity of M-NMPs was then assayed by measuring the inhibition of the photoreduction of nitro blue tetrazolium (NBT). Under UV irradiation, the mixture of riboflavin, methionine, and NBT would

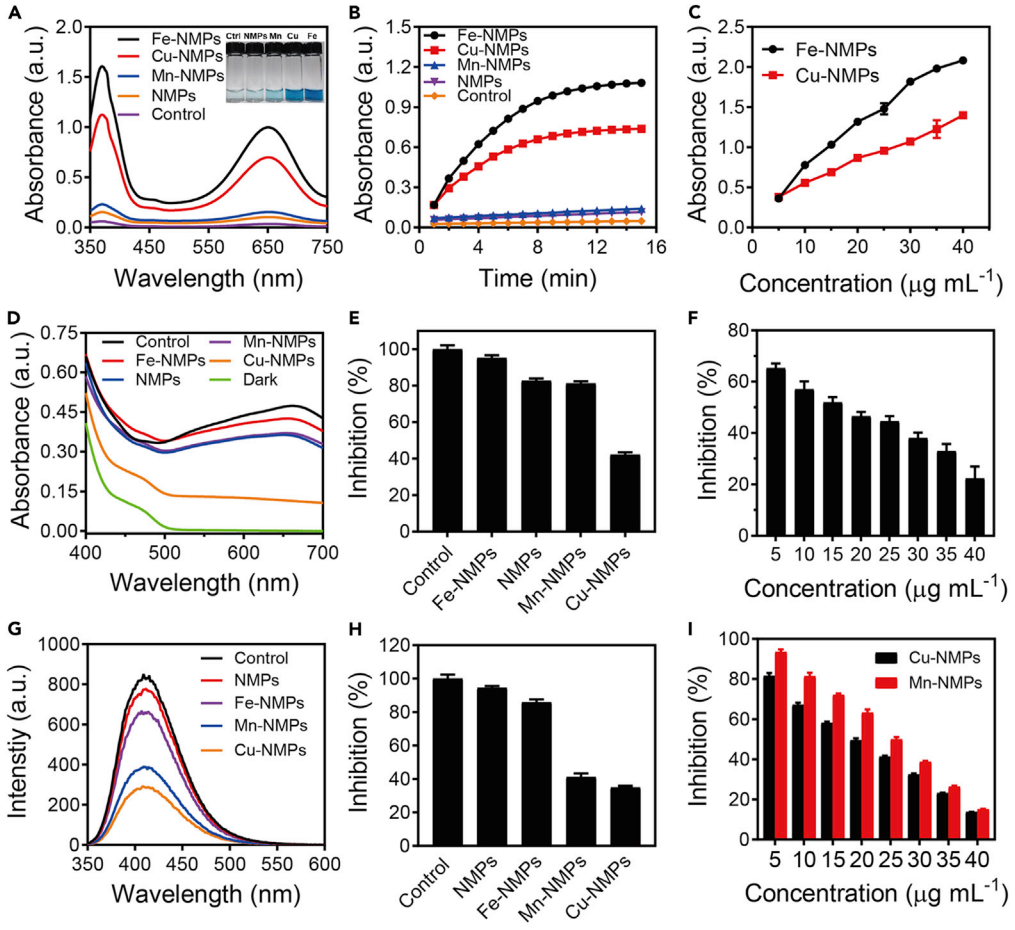

Figure 2. Enzyme-like Activities of M-NMPs

(A) POD-like activity of different M-NMPs. Insert shows the color change of TMB oxidation with various treatments.

(B) POD-like activity of different M-NMPs at different reaction time.

(C) Absorbance at 650 nm of the TMB oxidation with different concentrations of Fe-NMPs and Cu-NMPs.

(D) SOD-like activity of different M-NMPs.

(E) Inhibition rate of NBTphotooxidation for different M-NMPs.

(F) Inhibition rate of NBTphotooxidation with different concentrations of Cu-NMPs.

(G) CAT-like activity of M-NMPs.

(H) Inhibition rate of TA oxidation for different M-NMPs.

(I) Inhibition rate of TA oxidation with different concentrations of Cu-NMPs and Mn-NMPs. Results are expressed as the mean ± S.D. of at least three independent experiments measured in triplicate.

See also Figures S2–S5 and Table S2.

produce a high level of superoxide, leading to an obvious absorption at 650 nm (Fan et al., 2018). Thus, the SOD-like activity could be evaluated by the decrease of absorption at 650 nm. As shown in Figure 2D, the mixture in the control exhibited an obvious absorption at 650 nm, whereas a sharp decrease of absorption could be observed with Cu-NMPs treatment. In the presence of 20 μg mL^{-1} of Cu-NMPs, the superoxide scavenging rates could reach to 59.8%, manifesting its excellent SOD-like activity (Figure 2E). The SOD-like activity of catalyst in different concentrations was also tested, which is found to enhance as the concentration increase (Figure 2F). These results confirmed that the Cu-NMPs showed great SOD-like activity and could be used as efficient superoxide radical removal agents.

Previous studies have demonstrated that metal ion-containing materials could catalyze the decomposition of H_2O_2 such as CAT (Zhang et al., 2016). Here, the CAT-like activity of M-NMPs was also investigated by measuring the inhibition of the oxidation of non-fluorescent terephthalic acid (TA). In the presence of H_2O_2, TA could be oxidized to generate fluorescent 2-hydroxyterephthalic acid with an emission wavelength of

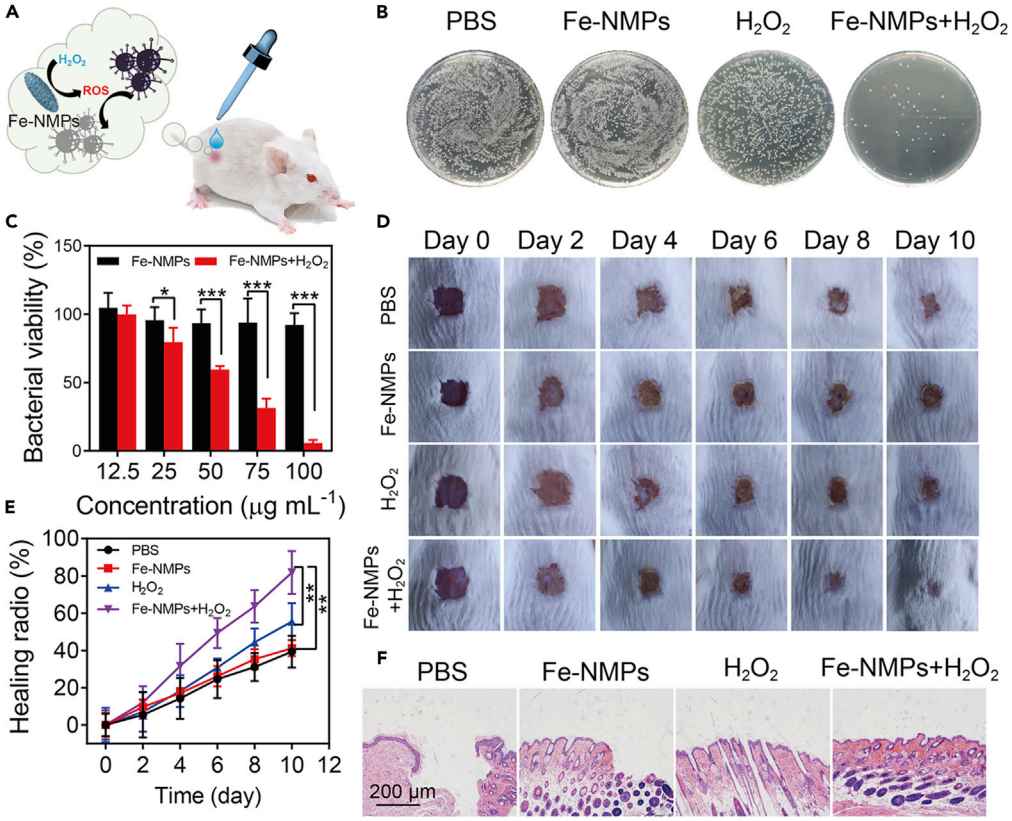

Figure 3. The Antibacterial Activity of Fe-NMPs against *S. aureus*

(A) Schematic of the antibacterial activity of Fe-NMPs against *S. aureus*.

(B) Photographs of bacterial colonies formed by *S. aureus* with different treatment.

(C) Bacterial viability of *S. aureus* with different treatment.

(D and E) Photographs (D) and the corresponding healing ratio (E) of *S. aureus*-infected wound with different treatment at different days.

(F) H&E analysis of the wounds with different treatment after 10 days of therapy. Significance between each group was calculated using ANOVA with Tukey post hoc test.

*p< 0.05, **p< 0.01, ***p< 0.001. Results are expressed as the mean ± S.D. of at least three independent experiments measured in triplicate.

425 nm (Yao et al., 2018). Therefore, the CAT-like activity of M-NMPs could be evaluated by the decrease of fluorescence intensity at 425 nm. With the treatment of Cu-NMPs and Mn-NMPs, a significant decrease of fluorescence intensity was observed, indicating that they could efficiently decompose the H_2O_2 (Figure 2G). And the decomposition rate could respectively reach to 65.7% and 60.4% with 30 μg mL^{-1} of Cu-NMPs and Mn-NMPs (Figure 2H). It was observed that the CAT-like activity enhanced with the increasing concentration of the catalysts (Figures 2I and S5). These results demonstrated that the Cu-NMPs and Mn-NMPs showed prominent CAT-like activity and could be used to eliminate the H_2O_2.

Antibacterial Property of Fe-NMPs *In Vitro* and *In Vivo*

Given the multienzyme-like activities of different M-NMPs, their potential applications in biomedical field were expected. Previous researches have shown that nanoparticles with POD-like property could catalyze H_2O_2 to form hydroxyl radicals (•OH) in the antibacterial applications (Xu et al., 2019). In view of the high POD-like activity of Fe-NMPs, its antibacterial property was explored (Figure 3A). Before that, the biocompatibility of the Fe-NMPs was evaluated by studying its cytotoxicity effect. According to Figure S6, Fe-NMPs exhibited good biocompatibility toward 3T3 cells, which guaranteed its applications in biomedicine. The *in vitro* antibacterial activity of Fe-NMPs toward *S. aureus* was firstly studied by using UV-vis spectrometry and plate counting method. As shown in Figure 3B, Fe-NMPs showed a good antibacterial activity toward *S. aureus* in the presence of H_2O_2 when compared with other groups. The same result was also

observed by UV-vis spectrometry (Figure 3C). These results indicated that Fe-NMPs displayed high anti-bacterial activity. And the *in vivo* bactericidal efficacy of Fe-NMPs was further evaluated by using wound infection model in mice. Mice with wound infection were randomly divided into four groups and treated with PBS, Fe-NMPs (100 μg mL^{-1}), H_2O_2 (100 μM), and Fe-NMPs + H_2O_2, respectively. After 10 days of treatment, the Fe-NMPs + H_2O_2-treated mice achieved 80.6% wound healing, whereas the controls only reached to 42.5% healing (Figures 3D and 3E). The wound healing efficiency was further verified by hematoxylin-eosin (H&E) staining (Figure 3F). Therefore, Fe-NMPs exhibited conspicuous anti-bacteria property in both *in vitro* and *in vivo* assays, revealing potential application in anti-bacterial and wound healing.

Radiotherapy Sensitization Effect of Mn-NMPs *In Vitro* and *In Vivo*

Nowadays, as one of the most common treatments for cancer in clinic, radiotherapy (RT) depends on the high-intensity ionizing radiation to activate tumor-dissolved oxygen to induced DNA damages for achieving cancer therapy (Lu et al., 2018). However, the inadequate oxygen supply in most solid tumors severely reduces the effectiveness of RT. Thus, developing methods to increase the oxygen content in the tumor tissues maybe quite a useful strategy to enhance the efficiency of RT. Catalytic decomposition of endogenous H_2O_2 could be an ideal strategy to increase the level of O_2 in tumors. To date, many studies have been reported to use catalysts for endogenous H_2O_2 decomposition to improve the hypoxia condition of tumors for cancer treatment (Chen et al., 2019; He et al., 2019; Song et al., 2018). In consideration of the CAT-like activity of Mn-NMPs, which could act as a catalyst for decomposition of H_2O_2 to generate O_2, we expected that Mn-NMPs could act as a radiosensitizer to enhance the efficiency of RT for cancer treatment (Figure 4A). Firstly, the ability of Mn-NMPs to decompose H_2O_2 to generate oxygen was studied by using dissolved oxygen meter. As expected, the O_2 concentration in Mn-NMPs group was obviously increased in the presence of H_2O_2 (Figure 4B), confirming that the Mn-NMPs is able to decompose H_2O_2 to generate O_2. Generally, the HIF-1α protein level could indicate the degree of hypoxia in cells, and the expression of HIF-1α protein would be upregulated when hypoxia. To evaluate the intracellular O_2 generation ability of Mn-NMPs, the expression of HIF-1α protein was detected by immunofluorescence staining. Relatively low HIF-1α protein level was observed in Mn-NMPs treated cells, suggesting that Mn-NMPs could effectively alleviate the hypoxia (Figure 4C). To further investigate whether Mn-NMPs could act as radiosensitizer toward cancer cells under hypoxia, the cellular survival assay was performed in B16-F10 cells. As shown in Figure 4D, after X-ray irradiation, cells treated with or without Mn-NMPs showed a similar cellular survival rate under normoxia, whereas the Mn-NMP- treated cells showed a significant decrease in cellular survival rate under hypoxia compared with the untreated group. Notably, Mn-NMP-treated cells could effectively enhance the efficacy of RT under hypoxia, revealing that Mn-NMPs could act as a radiosensitizer for cancer treatment.

To further evaluate the radiotherapy sensitization effect of Mn-NMPs *in vivo*, a melanoma tumor model was established to study the the radiotherapy sensitization effect of Mn-NMPs. Firstly, the O_2 generation ability of Mn-NMPs *in vivo* was studied by monitoring the saturated O_2 levels within tumors with photoacoustic (PA) imaging. As expected, the O_2 level was significantly increased at 6 h post-injection of Mn-NMPs (Figure 4E), indicating the ability of Mn-NMPs to decompose endogenous H_2O_2 into O_2 in tumor. And the HIF-1α protein expression level was also assessed by immunofluorescence staining to confirm the O_2 generation ability of Mn-NMPs. As exhibited in Figure 4F, the Mn-NMP-treated tumor showed relatively weak fluorescence of anti-HIF-1α antibody compared with the control, indicating the downregulation of HIF-1α expression through O_2 generation. These results indicated that the Mn-NMPs could relieve the tumor hypoxia through the decomposition tumor endogenous H_2O_2 into O_2. Next, the *in vivo* antitumor ability of Mn-NMPs was evaluated to study its radiotherapy sensitization effect. According to the tumor volume and the tumor weight evaluated on the 14th day, Mn-NMP-treated group showed unconspicuous therapeutic effect without X-ray irradiation. A slight tumor inhibition was observed with X-ray irradiation alone, whereas Mn-NMP-treated group showed an obvious inhibition of tumor growth with 92.6% tumor suppression under X-ray irradiation, suggesting superior radiotherapy sensitization effect of Mn-NMPs in hypoxia (Figures 4G and 4H). And the images of tumor size and the histologic section assays also confirmed the positive therapeutic effect of the radiosensitizer (Figures 4I and S7). No obvious body weight changes were observed during the treatment, and no abnormality was found in major organs after the treatment, illustrating little systemic toxicity of Mn-NMPs (Figures S8 and S9). These results suggested that Mn-NMPs could provide oxygen through decomposing endogenous H_2O_2 in tumors and act as a radiosensitizer to enhance RT efficacy.

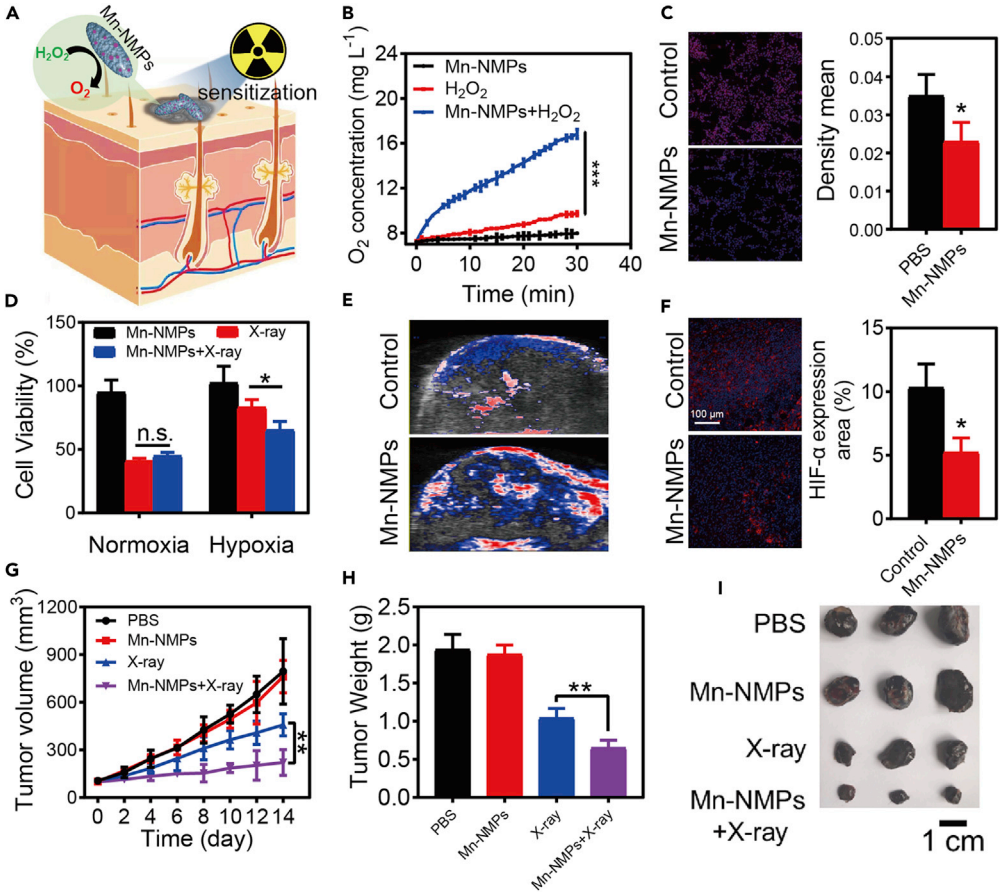

Figure 4. The Radiotherapy Sensitization Effect of Mn-NMPs in Cancer Therapy

(A) Schematic of the radiotherapy sensitization effect of Mn-NMPs in cancer therapy.

(B) Oxygen generation with different treatment.

(C) HIF-1α expression level in B16-F10 cells with or without the treatment of Mn-NMPs. The cell nuclei and HIF-1α were stained with DAPI (blue) and anti-HIF-1α antibody (red), respectively.

(D) Cell viability of B16-F10 cells with different treatments in normoxia or hypoxia.

(E) Representative PA images of B16-F10 tumors with or without the treatment of Mn-NMPs.

(F) Immunofluorescence images of B16-F10 tumor after different treatments. The cell nuclei and HIF-1α were stained with DAPI (blue) and anti-HIF-1α antibody (red), respectively.

(G–I) Tumor volume changes (G), tumor weight (H), and the photograph of the tumors (I) with different treatments.

Significance between each group was calculated using ANOVA with Tukey post hoc test. *$p < 0.05$, **$p < 0.01$, ***$p < 0.001$. Results are expressed as the mean ± S.D. of at least three independent experiments measured in triplicate.

See also Figures S6–S9.

Anti-inflammatory Effect of Cu-NMPs *In Vitro* and *In Vivo*

In human body, harmful superoxide radicals are transformed into H_2O_2 through SOD. And then the H_2O_2 is further decomposed into completely harmless water by CAT and POD. In this way, the three enzymes form a complete anti-oxidation chain to protect cells against oxidative damage (Huang et al., 2016). Given that the Cu-NMPs were verified to show the three enzyme-like activities of anti-oxidation chain simultaneously, we expected that the Cu-NMPs could rescue the oxidative stress and show the potential of remedying oxidation-related diseases. Inflammation, a disease linked to ROS-induced oxidative stress, could be alleviated by eliminating the harmful ROS (Zhang et al., 2019; Wan et al., 2017). So the anti-inflammation ability of Cu-NMPs was studied to assess its therapeutic potential in oxidation-related diseases (Figure 5A). Before that, the biocompatibility of the Cu-NMPs was evaluated by studying its cytotoxicity effect toward mouse macrophage cell line (RAW264.7). After incubating RAW264.7 with Cu-NMPs at different concentrations for 24 h, it was observed that the cell proliferation was hardly affected (Figure S10). This result demonstrated that Cu-NMPs possessed favorable biocompatibility and could be applied in biomedical applications. LPS, which exists as antigen in the outer membrane of bacteria, has been used

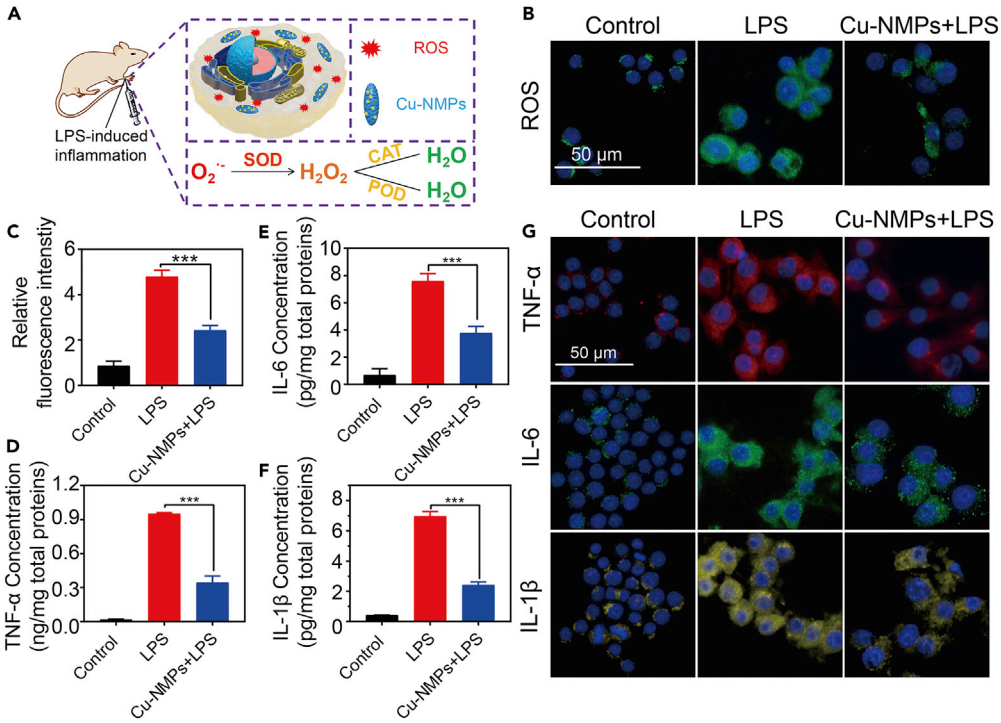

Figure 5. The Anti-inflammation Effect of Cu-NMPs toward RAW264.7Cells

(A) Schematic of the anti-inflammation effect of Cu-NMPs toward RAW264.7 cells.

(B) Fluorescence microscopy images of ROS level in RAW264.7 cells with different treatments.

(C) ROS level in RAW264.7 cells with different treatments.|

(D–F) The expression level of pro-inflammatory cytokines TNF-α (D), IL-6 (E), and IL-1β (F) in RAW264.7 cells with different treatments.

(G) Fluorescence microscopy images of pro-inflammatory cytokines TNF-α, IL-6, and IL-1β expression in RAW264.7 cells with different treatments. Significance between each group was calculated using ANOVA with Tukey post hoc test. ***$p < 0.001$, n.s. = not significant. Results are expressed as the mean ± S.D. of at least three independent experiments measured in triplicate. See also Figures S10–S15.

as a pattern in the induction of inflammation models. Here, the anti-inflammatory action of Cu-NMPs was examined on the LPS-induced inflammation of RAW264.7. Having been stimulated by LPS, the macrophages would produce an inflammatory reaction resulting in the excess production of ROS and the high expression level of pro-inflammatory cytokines such as TNF-α, IL-6, and IL-1β. The ROS level was analyzed by detecting the conversion of non-fluorescent 2′, 7′-dichlorofluoresceindiacetate (DCFH-DA) to strong fluorescent 2′, 7′-dichlorofluorescein (DCF) (Zhang et al., 2015). According to the fluorescence microscopy images in Figures 5B and S11, intense green fluorescence was observed in LPS-incubated RAW264.7. In contrast, after being treated with Cu-NMPs, the macrophages showed a dramatical decreased fluorescence, indicating the ROS scavenging capacity of the Cu-NMPs (Figure 5C). To further assess the anti-inflammation ability of Cu-NMPs, the expression of three pro-inflammatory cytokines, TNF-α, IL-6, and IL-1β, in RAW264.7 were quantified by enzyme-linked immunosorbent assay (ELISA). As shown in Figures 5D–5F, LPS treatment led to an overexpression of three pro-inflammatory cytokines in macrophages, which significantly decreased under the treatment of Cu-NMPs. With 40 μg mL^{-1} of Cu-NMPs treatment, the removal rate of TNF-α, IL-6, and IL-1β could reach to 65.1%, 55.5%, and 69.4%, respectively (Figure S12). Immunocytochemistry staining was also employed to measure the expression level of TNF-α, IL-6, and IL-1β. It was observed that LPS-stimulated overexpression of pro-inflammatory cytokines in macrophages were drastically reduced after the treatment of Cu-NMPs (Figures 5G and S13–S15). These *in vitro* results demonstrated that Cu-NMPs could effectively reduce inflammatory responses and so may have the potential to be applied in oxidation-related diseases.

We also established an inflammation model on BALB/c mice to further explore the potential application of Cu-NMPs in anti-inflammation *in vivo*. The inflammation model on paw of BALB/c mice was constructed by local

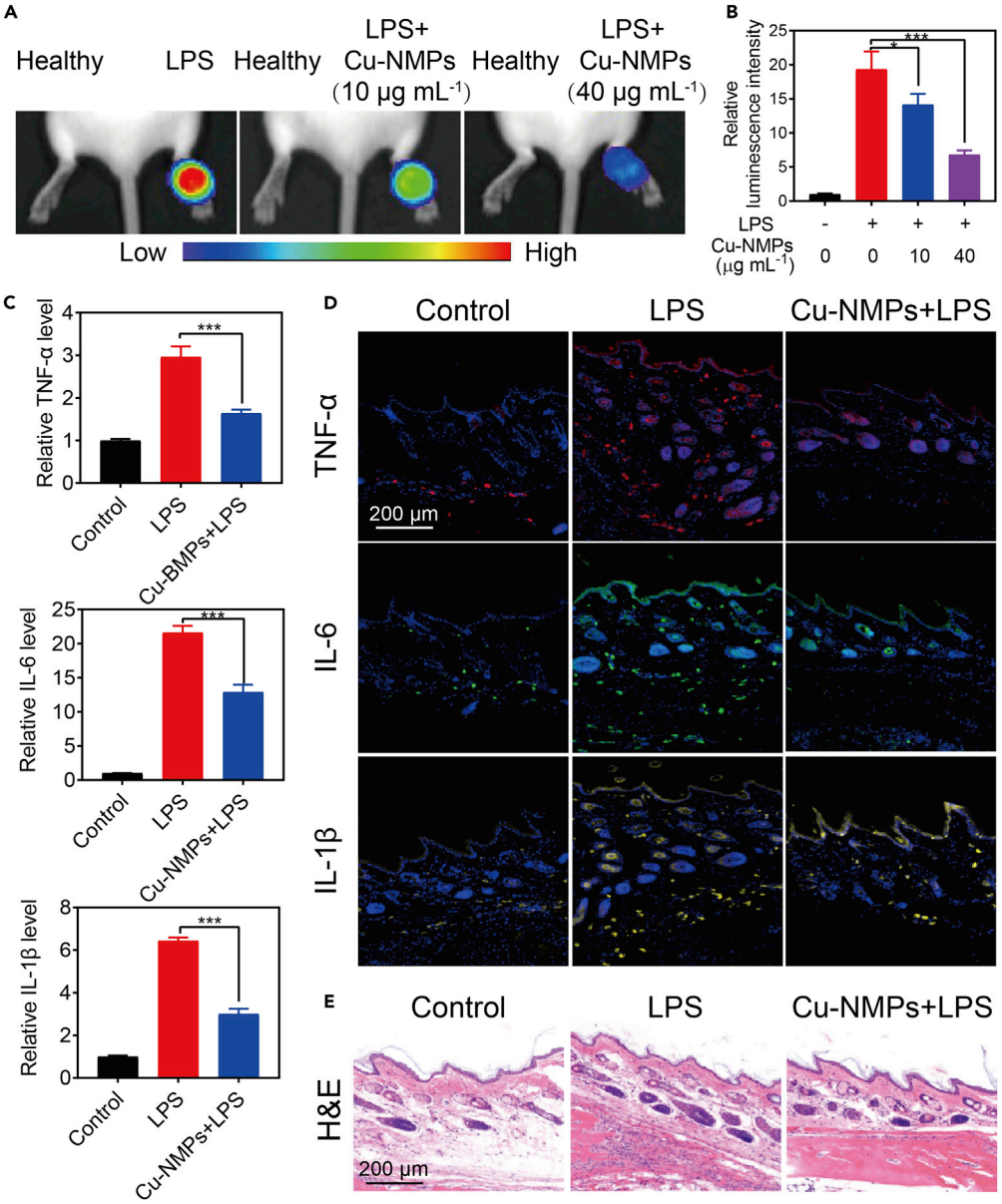

Figure 6. The Anti-inflammation Effect of Cu-NMPs on LPS-Induced Inflamed Paws

(A and B) *In vivo* bioluminescence imaging (A) and corresponding luminescence intensities (B) of ROS level in LPS-induced inflamed paws with different treatments.

(C) The expression level of pro-inflammatory cytokines TNF-α, IL-6, and IL-1β in LPS-induced inflamed paws with different treatments.

(D) Immunofluorescence staining of pro-inflammatory cytokines TNF-α, IL-6, and IL-1β expression in LPS-induced inflamed paws with different treatments.

(E) H&E staining images of LPS-induced inflamed paws of mice with different treatments. Significance between each group was calculated using ANOVA with Tukey post hoc test. *$p < 0.05$, ***$p < 0.001$. Results are expressed as the mean ± S.D. of at least three independent experiments measured in triplicate.

See also Figures S16–S20.

injection of LPS. The ROS level in paws was imaged by a luminescent probe. As displayed in Figures 6A and 6B, strong luminescence signal of ROS was detected in LPS-induced inflamed paws, whereas the ROS level obviously decreased in the presence of Cu-NMPs. It was found that the luminescence signal decreased progressively with the increasing concentrations of Cu-NMPs. Cu-NMPs showed 70.0% ROS removal rate at 40 μg mL^{-1}, revealing

an admirable ROS scavenging activity (Figure S16). To further evaluate the anti-inflammation ability of Cu-NMPs*in vivo*, the expression of TNF-α, IL-6, and IL-1β in LPS-induced inflammatory paw was quantified by ELISA. It was found that LPS-induced overexpression of pro-inflammatory cytokines were dramatically decreased with the treatment of Cu-NMPs (Figure 6C). A dose-dependent decrease in the expression of pro-inflammatory cytokines was also observed in mice treated with Cu-NMPs. The removal rate of the TNF-α, IL-6, and IL-1β could respectively reach to 96.7%, 67.2%, and 83.5% with 40 μg mL^{-1} of Cu-NMPs (Figure S17). Immunofluorescence staining was also used to visualize the expression of TNF-α, IL-6, and IL-1β in inflamed paws. Treatment with Cu-NMPs significantly reduced the LPS-induced pro-inflammatory cytokines levels, demonstrating the effectiveness of Cu-NMPs in inhibiting the production of inflammatory cytokines in tissue inflammation (Figures 6D and S18–S20). H&E staining was also assayed to measure the infiltration of the inflammatory cells. A markedly enhanced infiltration of the inflammatory cells was observed in inflamed paws, which was significantly decreased after the treatment of Cu-NMPs (Figure 6E). These *in vivo* results demonstrated that Cu-NMPs could effectively reduce inflammatory responses, showing the possibility of applying in oxidation-related diseases.

Limitations of the Study

M-NMPs based on the human hairs succeeded in mimicking natural enzymes and exhibited some catalytic activities. However, what cannot be ignored is the variability of hair samples. In this study, the hair samples we used were mainly the hairs of yellow race obtained from nearby barbershop. The hairs in different racial types have different constitutions and constructions (Imai et al., 2016; Liu et al., 2005), which may possess different activity from our enzyme-like system. Owing to the lack of the hair samples from different racial types, the activity of enzyme-like system derived from other hair samples were not studied. Furthermore, the refined structure and catalytic mechanism of M-NMPs need to be further explored for better understanding the catalytic mechanism. Besides, as an enzyme-like system, the selectivity of the mimic enzyme appears to be particularly important and the ability of selective catalysis for this enzyme-like system should be improved.

In summary, a novel natural enzyme alternative was prepared by binding different metal ions into NMPs extracted from human hair. The different M-NMPs exhibited different enzyme-like activities. The Fe-NMPs and Mn-NMPs showed outstanding POD-like activity and CAT-like activity respectively. In addition, the Cu-NMPs could serve as combined POD, SOD, and CAT alternatives to mimic anti-oxidation chain to eliminate ROS. The enzyme-active M-NMPs have the potential to be applied in the biomedical application. Both *in vitro* and *in vivo* antibacterial activity assays demonstrated that Fe-NMPs possessed the potential in antibacterial applications. Besides, Mn-NMPs with CAT-like activity exhibited a remarkable radiotherapy sensitization effect in cancer therapy. Furthermore, Cu-NMPs showed three enzyme-like activities of anti-oxidation chain simultaneously and could rescue the oxidative stress to protect cells against oxidative damage with the potential of remedying oxidation-related diseases. Anyway, this study might provide new perspectives on developing enzyme alternatives with multifunctionality to meet various requirements in biomedical applications.

METHODS

All methods can be found in the accompanying Transparent Methods supplemental file.

SUPPLEMENTAL INFORMATION

Supplemental Information can be found online at https://doi.org/10.1016/j.isci.2019.100778.

ACKNOWLEDGMENTS

This work was supported by the National Natural Science Foundation of China (51833007, 51690152, 51573142, and 21721005).

AUTHOR CONTRIBUTIONS

S.H. and X.Z.Z. conceived the project and designed the experiments. S.H. and Q.L.Z. synthesized materials and probes. Q.L.Z. and J.J.Y performed *in vitro* experiments. S.H. and C.Z. collected and analyzed the data. S.H. and D.W.Z. performed *in vivo* experiments. S.H., Q.L.Z., D.W.Z., C.Z., Y.Z., H.C., and X.Z.Z. co-wrote the manuscript. All authors discussed the results and reviewed the manuscript.

DECLARATION OF INTERESTS

The authors declare no competing interests.

Received: November 1, 2019
Revised: November 27, 2019
Accepted: December 12, 2019
Published: January 24, 2020

REFERENCES

Chen, W.-H., Vázquez-González, M., Zoabi, A., Abu-Reziq, R., and Willner, I. (2018). Biocatalytic cascades driven by enzymes encapsulated in metal-organic framework nanoparticles. Nat. Catal. *1*, 689–695.

Chen, Y., Zhong, H., Wang, J., Wan, X., Li, Y., Pan, W., Li, N., and Tang, B. (2019). Catalase-like metal-organic framework nanoparticles to enhance radiotherapy in hypoxic cancer and prevent cancer recurrence. Chem. Sci. *10*, 5773–5778.

Cho, S., Shim, T.S., Kim, J.H., Kim, D.-H., and Kim, S.-H. (2017). Selective coloration of melanin nanospheres through resonant mie scattering. Adv. Mater. *29*, 1700256.

Das, A., and Hecht, M.H. (2007). Peroxidase activity of de novo heme proteins immobilized on electrodes. J. Inorg. Biochem. *101*, 1820–1826.

D'Ischia, M., Napolitano, A., Ball, V., Chen, C.-T., and Buehler, M.J. (2014). Polydopamine and eumelanin: from structure-property relationships to a unified tailoring strategy. Acc. Chem. Res. *47*, 3541–3550.

Fan, K., Cao, C., Pan, Y., Lu, D., Yang, D., Feng, J., Song, L., Liang, M., and Yan, X. (2012). Magnetoferritin nanoparticles for targeting and visualizing tumour tissues. Nat. Nanotechnol. *7*, 459–464.

Fan, K., Xi, J., Fan, L., Wang, P., Zhu, C., Tang, Y., Xu, X., Liang, M., Jiang, B., Yan, X., et al. (2018). *In vivo* guiding nitrogen-doped carbon nanozyme for tumor catalytic therapy. Nat. Commun. *9*, 1440.

Gao, L., Zhuang, J., Nie, L., Zhang, J., Zhang, Y., Gu, N., Wang, T., Feng, J., Yang, D., Perrett, S., et al. (2007). Intrinsic peroxidase-like activity of ferromagnetic nanoparticles. Nat. Nanotechnol. *2*, 577–583.

He, Z., Huang, X., Wang, C., Li, X., Liu, Y., Zhou, Z., Wang, S., Zhang, F., Wang, Z., Jacobson, O., et al. (2019). A catalase-like metal-organic framework nanohybrid for O_2-evolving synergistic chemoradiotherapy. Angew. Chem. Int. Ed. *131*, 8844–8848.

Huang, P., Feng, L., Oldham, E.A., Keating, M.J., and Plunkett, W. (2000). Superoxide dismutase as a target for the selective killing of cancer cells. Nature *407*, 390–395.

Huang, Y., Liu, Z., Liu, C., Ju, E., Zhang, Y., Ren, J., and Qu, X. (2016). Self-assembly of multi-nanozymes to mimic an intracellular antioxidant defense system. Angew. Chem. Int. Ed. *128*, 6758–6762.

Imai, T., Higuchi, K., Yamamoto, Y., Arai, S., Nakano, T., and Tanaka, N. (2016). Sub-nm 3D observation of human hair melanin by high-voltage STEM. Microscopy (Oxf.) *65*, 185–189.

Kim, C.K., Kim, T., Choi, I.-Y., Soh, M., Kim, D., Kim, Y.-J., Jang, H., Yang, H.-S., Kim, J.Y., Park, H.-K., et al. (2012). Ceria nanoparticles that can protect against ischemic stroke. Angew. Chem. Int. Ed. *51*, 11039–11043.

Li, S.-Y., Cheng, H., Xie, B.-R., Qiu, W.-X., Zeng, J.-Y., Li, C.-X., Wan, S.-S., Zhang, L., Liu, W.-L., and Zhang, X.-Z. (2017a). Cancer cell membrane camouflaged cascade bioreactor for cancer targeted starvation and photodynamic therapy. ACS Nano *11*, 7006–7018.

Li, W., Liu, Z., Liu, C., Guan, Y., Ren, J., and Qu, X. (2017b). Manganese dioxide nanozymes as responsive cytoprotective shells for individual living cell encapsulation. Angew. Chem. Int. Ed. *56*, 13661–13665.

Liu, Y., Hong, L., Wakamatsu, K., Ito, S., Adhyaru, B., Cheng, C.-Y., Bowers, C.R., and Simon, J.D. (2005). Comparison of structural and chemical properties of black and red human hair melanosomes. Photochem. Photobiol. *81*, 135–144.

Lu, N., Fan, W., Yi, X., Wang, S., Wang, Z., Tian, R., Jacobson, O., Liu, Y., Yung, B.C., Zhang, G., et al. (2018). Biodegradable hollow mesoporousorganosilicananotheranostics for mild hyperthermia-induced bubble-enhanced oxygen-sensitized radiotherapy. ACS Nano *12*, 1580–1591.

Lu, Y., Yeung, N., Sieracki, N., and Marshall, N.M. (2009). Design of functional metalloproteins. Nature *460*, 855–862.

Mostert, A.B., Rienecker, S.B., Noble, C., Hanson, G.R., and Meredith, P. (2018). Thephotoreactive free radical in eumelanin. Sci. Adv. *4*, eaaq1293.

Robinson, N.J., and Winge, D.R. (2010). Copper metallochaperones. Annu. Rev. Biochem. *79*, 537–562.

Song, X., Xu, J., Liang, C., Chao, Y., Jin, Q., Wang, C., Chen, M., and Liu, Z. (2018). Self-supplied tumor oxygenation through separated liposomal delivery of H_2O_2 and catalase for enhanced radio-immunotherapy of cancer. Nano Lett. *18*, 6360–6368.

Triplett, T.A., Garrison, K.C., Marshall, N., Donkor, M., Blazeck, J., Lamb, C., Qerqez, A., Dekker, J.D., Tanno, Y., Lu, W.-C., et al. (2018). Reversal of indoleamine 2,3-dioxygenase-mediated cancer immune suppression by systemic kynurenine depletion with a therapeutic enzyme. Nat. Biotechnol. *36*, 758.

Wang, H., Wan, K., and Shi, X. (2018). Recent advances in nanozyme research. Adv. Mater. *31*, e1805368.

Wang, X., Hu, Y., and Wei, H. (2016). Nanozymes in bionanotechnology: from sensing to therapeutics and beyond. Inorg. Chem. Front. *3*, 41–60.

Wei, H., and Wang, E. (2013). Nanomaterials with enzyme-like characteristics (nanozymes): next-generation artificial enzymes. Chem. Soc. Rev. *42*, 6060–6093.

Wan, W.-L., Lin, Y.-J., Chen, H.-L., Huang, C.-C., Shih, P.-C., Bow, Y.-R., Chia, W.-T., and Sung, H.-W. (2017). *In situ*nanoreactor for photosynthesizing H_2 gas to mitigate oxidative stress in tissue inflammation. J. Am. Chem. Soc. *139*, 12923–12926.

Wu, Q., He, Z., Wang, X., Zhang, Q., Wei, Q., Ma, S., Ma, C., Li, J., and Wang, Q. (2019). Cascade enzymes within self-assembled hybrid nanogel mimicked neutrophil lysosomes for singlet oxygen elevated cancer therapy. Nat. Commun. *10*, 240.

Xu, B., Wang, H., Wang, W., Gao, L., Li, S., Pan, X., Wang, H., Yang, H., Meng, X., Wu, Q., et al. (2019). A single-atom nanozyme for wound disinfection applications. Angew. Chem. Int. Ed. *58*, 4911–4916.

Yang, B., Chen, Y., and Shi, J. (2019). Nanocatalytic medicine. Adv. Mater. *31*, 1901778.

Yang, W., Shi, X., Shi, Y., Yao, D., Chen, S., Zhou, X., and Zhang, B. (2018). Beyond the roles in biomimetic chemistry: an insight into the intrinsic catalytic activity of an enzyme for tumor-selective phototheranostics. ACS Nano *12*, 12169–12180.

Yao, J., Cheng, Y., Zhou, M., Zhao, S., Lin, S., Wang, X., Wu, J., Li, S., and Wei, H. (2018). ROS scavenging Mn_3O_4nanozymes for *in vivo* anti-inflammation. Chem. Sci. *9*, 2927–2933.

Zastrow, M.L., Peacock, A.F.A., Stuckey, J.A., and Pecoraro, V.L. (2011). Hydrolytic catalysis and structural stabilization in a designed metalloprotein. Nat. Chem. *4*, 118–123.

Zhang, B., Wang, F., Zhou, H., Gao, D., Yuan, Z., Wu, C., and Zhang, X. (2019). Polymer dots compartmentalized in liposomes as a photocatalyst for *in situ* hydrogen therapy. Angew. Chem. Int. Ed. *58*, 2744–2748.

Zhang, Q., Zhao, K., Shen, Q., Han, Y., Gu, Y., Li, X., Zhao, D., Liu, Y., Wang, C., Zhang, X., et al. (2015). Tet2 is required to resolve inflammation by recruiting hdac2 to specifically repress IL-6. Nature *525*, 389.

Zhang, W., Hu, S., Yin, J.-J., He, W., Lu, W., Ma, M., Gu, N., and Zhang, Y. (2016). Prussian blue nanoparticles as multienzymemimetics and reactive oxygen species scavengers. J. Am. Chem. Soc. *138*, 5860–5865.

Zheng, D.-W., Hong, S., Xu, L., Li, C.-X., Li, K., Cheng, S.-X., and Zhang, X.-Z. (2018). Hierarchical micro-/nanostructures from human hair for biomedical applications. Adv. Mater. *30*, 1800836.

ISCI, Volume *23*

Supplemental Information

Enzyme Mimicking Based on the Natural Melanin Particles from Human Hair

Sheng Hong, Qiu-Ling Zhang, Di-Wei Zheng, Cheng Zhang, Yu Zhang, Jing-Jie Ye, Han Cheng, and Xian-Zheng Zhang

Transparent Methods

Materials

Hydrogen peroxide (H_2O_2) were obtained from Sigma. Riboflavin was purchased from Sinopharm Chemical Reagent Co., Ltd. Methionine, glutathione (GSH), 3,5,3',5'-tetramethylbenzidine (TMB) and terephthalic acid (TA) were purchased from Aladdin Industrial Corporation. Nitrotetrazolium blue chloride (NBT) were purchased from Meryer (Shanghai) Chemical Technology Co., Ltd. Hoechst 33342 and DAPI were purchased from Thermofisher Scientific. 3-(4,5-dimethyl-2-thiazolyl)-2,5-diphenyl-2-H-tetrazolium bromide (MTT) assay were purchased from Beyotime Biotechnology. The hairs were obtained from the barber shop nearby.

Preparation of NMPs and M-NMPs

The NMPs were prepared according to our previous work. Briefly, 5 g human hair was dissolved in 50 mL NaOH solution (1 M) and heated to 85^{o}C for 5 min. Then, the dark coloured solution was dialyzed against PBS for several times. Next, the NMPs were obtained by differential centrifugation with 200 g for 6 min to remove large residues and 1200 g for 10 min to gather the products. Finally, the NMPs were washed with DI water for several times and dried for later use.

The M-NMPs were prepared as follows. The prepared NMPs were stirred in 100 mM NaC1 solutions contained 10 mM corresponding metal ions at room temperature for 12 h. The metal-bound NMPs were obtained by centrifugation and dried for later use.

POD-like activity of M-NMPs

The POD-like activity of M-NMPs was performed in HAc-NaAc buffer solution (pH 3.6) by studying the oxidation of TMB with H_2O_2. Typically, the oxidation of TMB

was carried out in a mixture of M-NMPs solution (1 mg mL^{-1}, 20 μL), H_2O_2 (30%, 120 μL), TMB (10 mg mL^{-1}, 40 μL) in HAc-NaAc buffer solution with final volume of 1 mL. The absorbance of the mixture at 650 nm was recorded continuously at different reaction time. The UV-Vis absorption spectrum of the mixture was measured at 10 min of the reaction. And the change in color was photographed in the end of the reaction. The concentration dependence of catalysis was studied gradually from 5 μg mL^{-1} to 40 μg mL^{-1} of M-NMPs. The POD-like catalytic stability was assayed at different pH (2-8) and temperature (20-70 ^{o}C) conditions. The absorbance of the mixture at 650 nm with different pH and temperature was recorded.

The steady-state kinetic assays were conducted in 200 μL buffer solution with Fe-NMPs and Cu-NMPs as catalyst in the presence of different concentrations of H_2O_2 and TMB. The kinetic assays with TMB as the substrate were performed by the mixture of catalyst (10 μg mL^{-1}), 30% H_2O_2 (24 μL) and different concentrations of TMB solution (41.6, 83.2, 166.4, 249.6, 332.8, 416.0, 520.0, 624.0, 728.0, 832.0 μM). And the kinetic assays with H_2O_2 as the substrate were performed by the mixture of catalyst (10 μg mL^{-1}), TMB (10 mg mL^{-1}, 10 μL) and different concentrations of H_2O_2 (0.0441, 0.0882, 0.1764, 0.2646, 0.3528, 0.441, 0.5292, 0.6174, 0.7056, 0.882, 1.323, 1.764 M). The absorbance of the reactions at 650 nm was recorded continuously at different reaction time. And the Michaelis-Menten constant was calculated according to the Michaelis-Menten saturation curve fitting by GraphPad Prism 7.

SOD-like activity of M-NMPs

The SOD-like activity of M-NMPs was tested by measuring the inhibition of the photoreduction of NBT. In brief, the M-NMPs mixed with riboflavin (20 μM), methionine (13 mM), NBT (75 μM) in PBS (25 mM, pH 7.4) were illuminated by UV light for 10 min. After that, the UV-Vis absorption spectrum of the mixture was

measured. The mixture treated without M-NMPs and kept in the dark were served as the control and the blank, respectively. The inhibition rate was calculated by the equation: inhibition rate (%) = $[(A_0-A)/A_0] \times 100$ (A_0 and A refer to the absorbance of the control and the sample, respectively).

CAT-like activity of M-NMPs

The CAT-like activity of Cu-NMPs was analyzed by measuring inhibition of the generation of highly fluorescent 2-hydroxyterephthalic acid from non-fluorescent TA. In the presence of H_2O_2, TA could be oxidized to generate fluorescent 2-hydroxyterephthalic acid with a fluorescence signal at 425 nm upon excitation wavelength of 320 nm. The mixture containing M-NMPs, TA (0.5 mM) and H_2O_2 (10 mM) in PBS (25 mM, pH 7.4) were incubated for 24 h at room temperature. The fluorescence spectrum of mixture was then measured with an excitation wavelength of 320 nm.

Bacterial culture

Staphylococcus aureus (ATCC 25923) were cultured in Luria-Bertani (LB) medium at 37 ^{o}C. The LB medium contained 10 mg mL^{-1} tryptone, 5 mg mL^{-1} yeast extract and 0.5 mg mL^{-1} NaCl.

***In vitro* antibacterial experiments**

Firstly, UV–vis spectroscopy was performed to evaluate the antibacterial property of Fe-NMPs against *S. aureus*. Briefly, the *S. aureus* suspension were added into each well of a 96 well plate and separately treated with PBS, different concentration of Fe-NMPs and Fe-NMPs + H_2O_2. After incubation at 37 ^{o}C for 8 h, the absorbance of the suspension at 600 nm was measured to assess the bacterial viability.

The antibacterial effect of Fe-NMPs was also studied with plate counting method. *S. aureus* in different four groups were treated with PBS, Fe-NMPs (50 μg mL^{-1}),

H_2O_2 (100 μM) and Fe-NMPs + H_2O_2, respectively. The mixtures were then reacted for 30 min followed by placing on the LB solid medium and incubated for another 24 h. Counting the number of colonies in each group. All experiments were repeated three times.

Cell culture

RAW264.7 cells were cultured in 1640 medium with 5% CO_2 at 37 ^oC. B16-F10 cells were cultured in DMEM medium with 5% CO_2 at 37 ^oC. The 1640 medium and DMEM medium contained 10% heat-inactivated FBS and 1% antibiotics (penicillin-streptomycin, 10000 U mL^{-1}).

***In vitro* cell viability**

The *in vitro* cytotoxicity of Mn-NMPs against B16-F10 cells was detected by MTT assay. The B16-F10 cells were seeded in 96 well plates and followed by incubated with Fe-NMPs. 24 h later, the cells were treated with X-ray radiation (4 Gy). After 24 h post-irradiation, 20 μL of MTT (5 mg mL^{-1}) was added into each well and incubated for another 4 h. Subsequently, the culture medium containing MTT was replaced with DMSO (150 μL and the absorbance at 570 nm was determined using a microplate reader. The relative cell viability was calculated.

The *in vitro* cytotoxicity of Cu-NMPs towards RAW264.7 cells was also detected by MTT assay. RAW264.7 cells were seeded in 96-well plates (5×10^4 cells per well). 24 h later, the cells were incubated with Cu-NMPs at various concentrations (0, 0.625, 1.25, 2.5, 5, 10, 20, 40 μg mL^{-1}). Following incubation for another 24 h, the cell viability was evaluated using a MTT assay.

***In vitro* cytokines production**

The anti-inflammation ability of Cu-NMPs was studied by the measuring the expression level of pro-inflammatory cytokines TNF-α, IL-6 and IL-1β in

LPS-stimulated RAW264.7 cells. The RAW264.7 cells were seeded in 6-well plates. After 24 h of growth, the cells were treated with LPS for 6 h for inducing a inflammatory reaction. Afterwards, the LPS-induced cells were treated with Cu-NMPs. The supernatant was then collected and analyzed by ELISA to quantify the levels of TNF-α, IL-6 and IL-1β in each sample. And the expression levels of three pro-inflammatory cytokines were also visualized using immunocytochemical staining. After being washed with PBS for several times, the cells were fixed with 4% formaldehyde. The fixed cells were then stained with the antibodies for the three cytokines and DAPI. The images were observed by using CLSM.

Animal

Experimental protocols were approved by the Institutional Animal Care and Use Committee (IACUC) of the Animal Experiment Center of Wuhan University (Wuhan, China). All animal experimental procedures were performed in accordance with the Regulations for the Administration of Affairs Concerning Experimental Animals approved by the State Council of People's Republic of China.

***In vivo* wound model and antibacterial effect**

The antibacterial effect of Fe-NMPs was performed by wound infection model on female Balb/c mice. A wound of d = 10 mm was created on the back of the mice by surgery followed by injection of 10^8 CFU *S. aureus* to the wounds to build the wound infection model. The mice with infected wounds were divided into four groups (five mice per group) and treated with PBS, Fe-NMPs (100 μg mL^{-1}), H_2O_2 (100 μM) and Fe-NMPs + H_2O_2 through subcutaneous injection, respectively. The wounds were photographed every two days. After 10 days of treatments, the mice were sacrificed and the wound tissues were harvested and analyzed by H&E staining.

***In vivo* antitumoral effect**

The B16-F10 melanoma model was used as an example to evaluate the *in vivo* antitumoral effect. B16-F10 cells (1×10^6) in 100 μL of PBS were injected subcutaneously into the back of C57 male mice. When the size of tumor reached ~ 100 mm^3, the mice were randomly divided into four groups (five mice per group) and treated with PBS, Mn-NMPs, X-ray and Mn-NMPs+X-ray through subcutaneous injection, respectively. The X-ray irradiation (8 Gy) was carried out after Mn-NMPs injection for 12 h. The tumor sizes and body weights were measured every day for 14 days post-treatment.

***In vivo* inflammation models and anti-inflammatory effect**

The inflammation models on paw of BALB/c mice were constructed by local injection of LPS (20 μL, 2 mg mL^{-1}) in the paws of mice. After 6 h stimulation, the paws were treated with Cu-NMPs through subcutaneous injection (five mice per group). The levels of ROS in the inflamed paws were imaged by bioluminescence imaging on an IVIS imaging system. And the expression levels of pro-inflammatory cytokines TNF-α, IL-6 and IL-1β in the inflamed paws were also analyzed by ELISA.

Statistical analysis and sample collection

Significance among more than two groups was calculated using ANOVA Turkey's test by using SPSS 22.0. For cell experiments and *in vivo* experiments, investigators performing operations were blinded to treatment groups. In *in vivo* experiments, animals were randomly divided into different groups.

148 **Supplemental Figures**

149

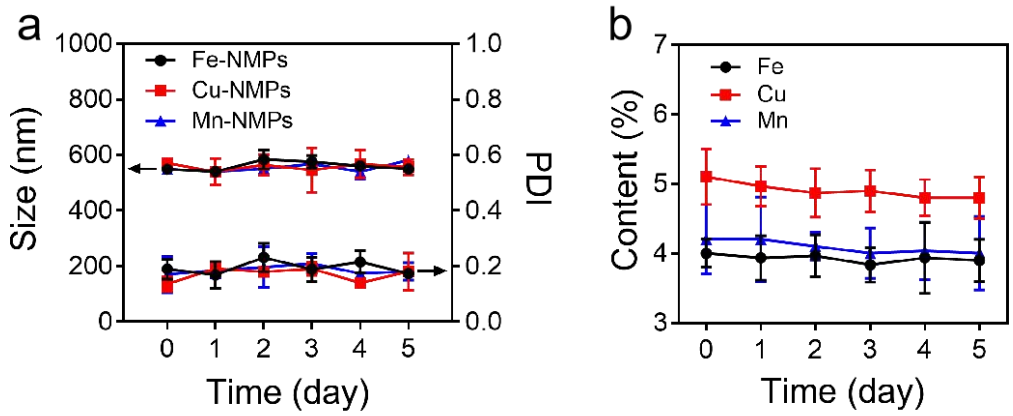

150

151 **Figure S1.** Related to **Figure 1.** The stability of M-NMPs. (a) Mean size and PDI of

152 M-NMPs in 5 days. (b) Metal content of M-NMPs in 5 days.

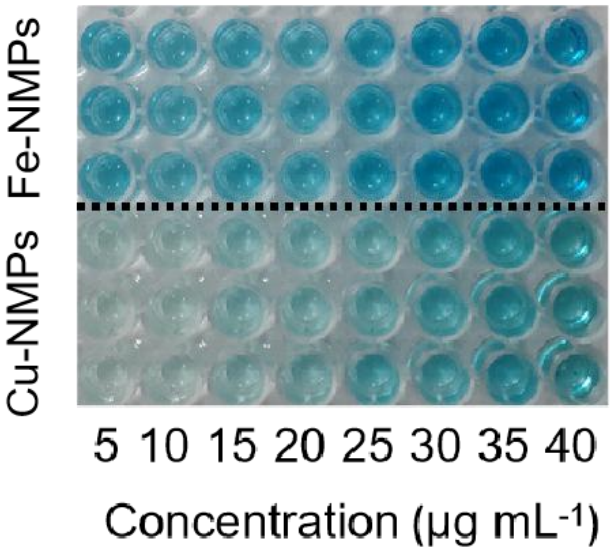

153

154 **Figure S2.** Related to **Figure 2.** The color changes of the TMB oxidation with

155 different concentrations of Fe-NMPs and Cu-NMPs.

156

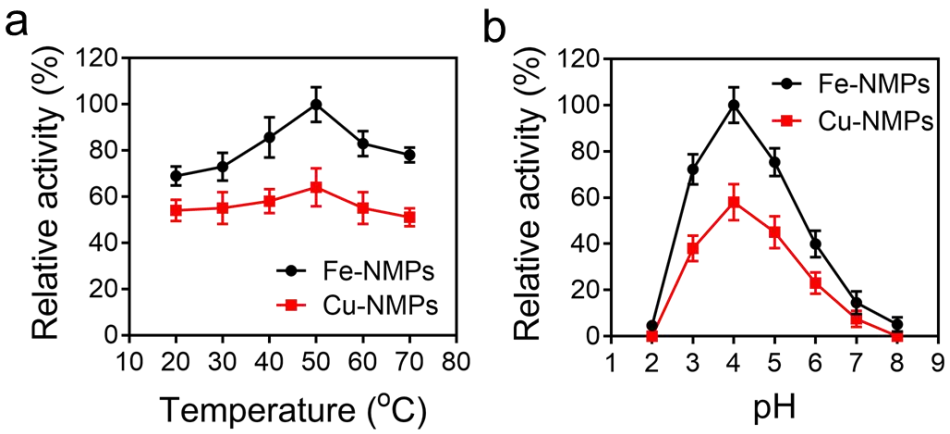

Figure S3. Related to **Figure 2.** Characterization for POD-like activity. The relative POD-like activity of Fe-NMPs and Cu-NMPs at different temperature (a) and different pH (b). Results are expressed as the mean ± S.D. of at least three independent experiments measured in triplicate.

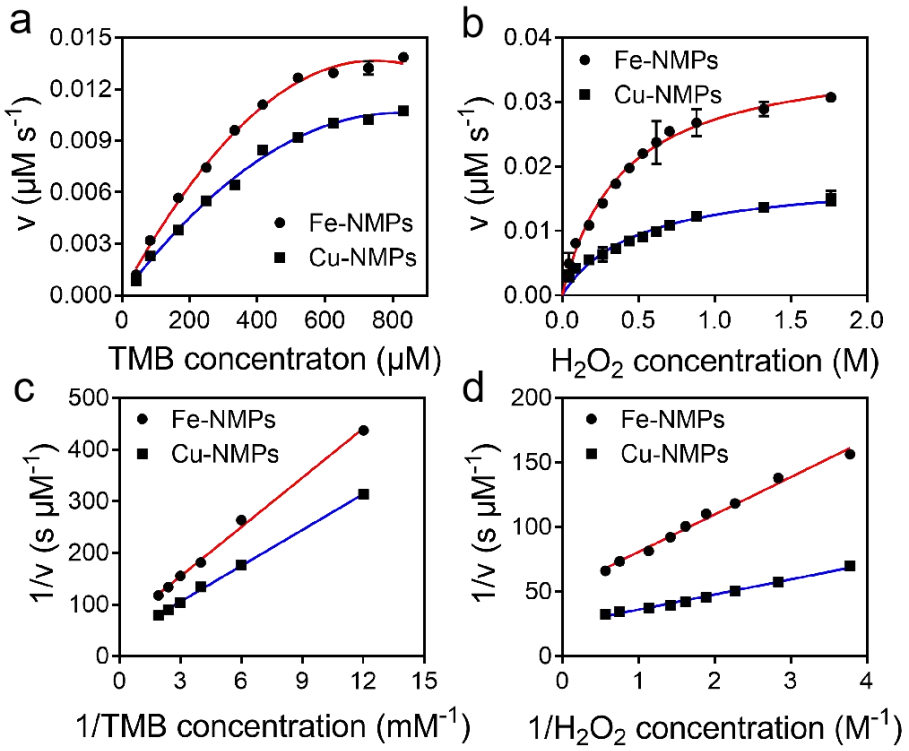

163

164 **Figure S4.** Related to **Figure 2.** The steady-state kinetic assays of Fe-NMPs and

165 Cu-NMPs as catalysts and different concentrations of H_2O_2 and TMB as substrates.

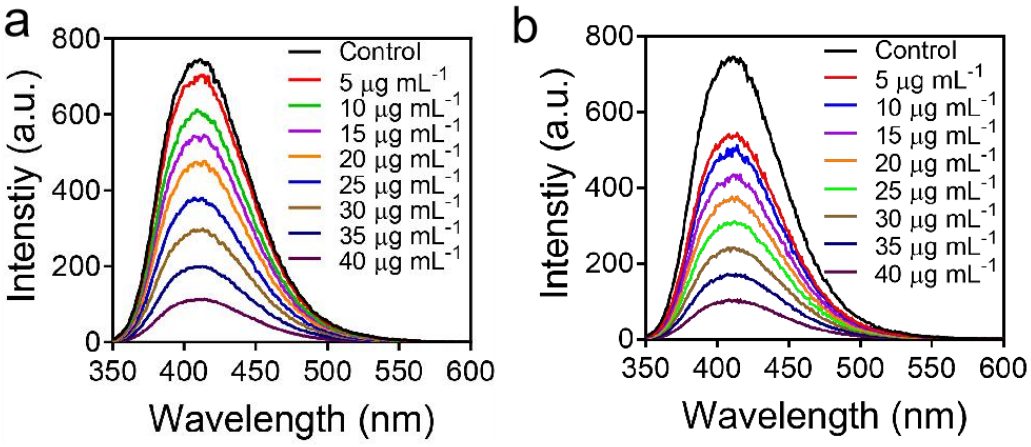

166

167 **Figure S5.** Related to **Figure 2.** The decomposition efficiency of H_2O_2 in presence of

168 different concentrations of Mn-NMPs (a) and Cu-NMPs (b).

169

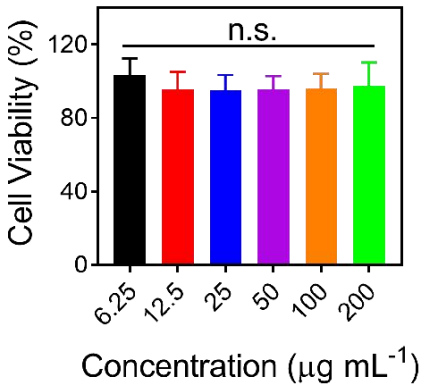

170

171 **Figure S6.** Related to **Figure 4.** Cell viability of 3T3 cells with the treatment of

172 different concentration of Fe-NMPs.

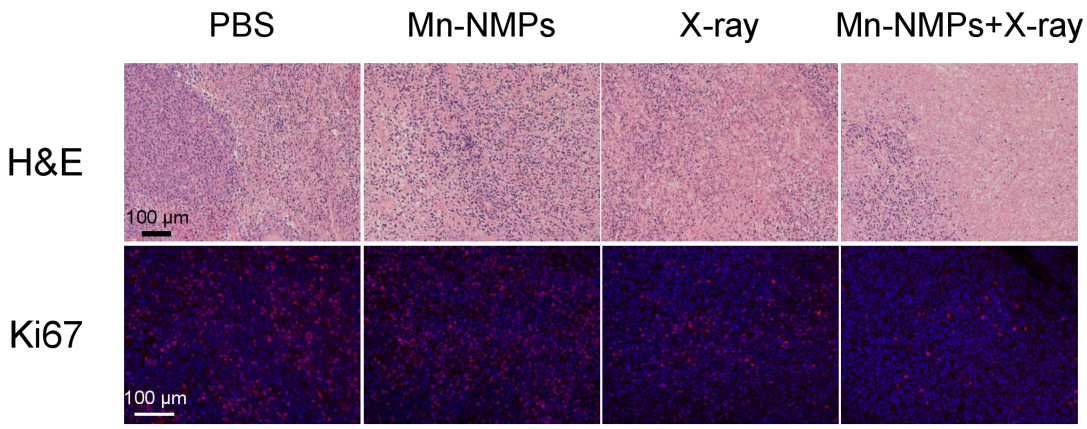

Figure S7. Related to **Figure 4.** H&E and Ki67 immunofluorescence staining of B16-F10 tumor tissues with different treatment.

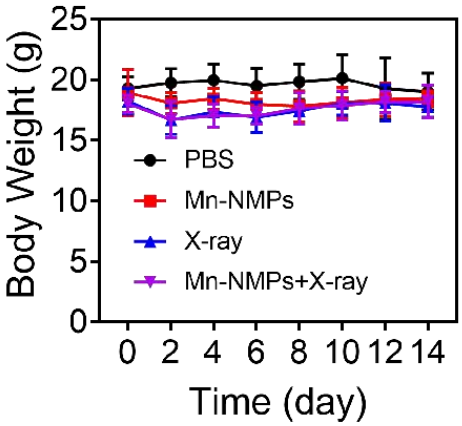

Figure S8. Related to **Figure 4.** Body weight changes of mice with different treatment.

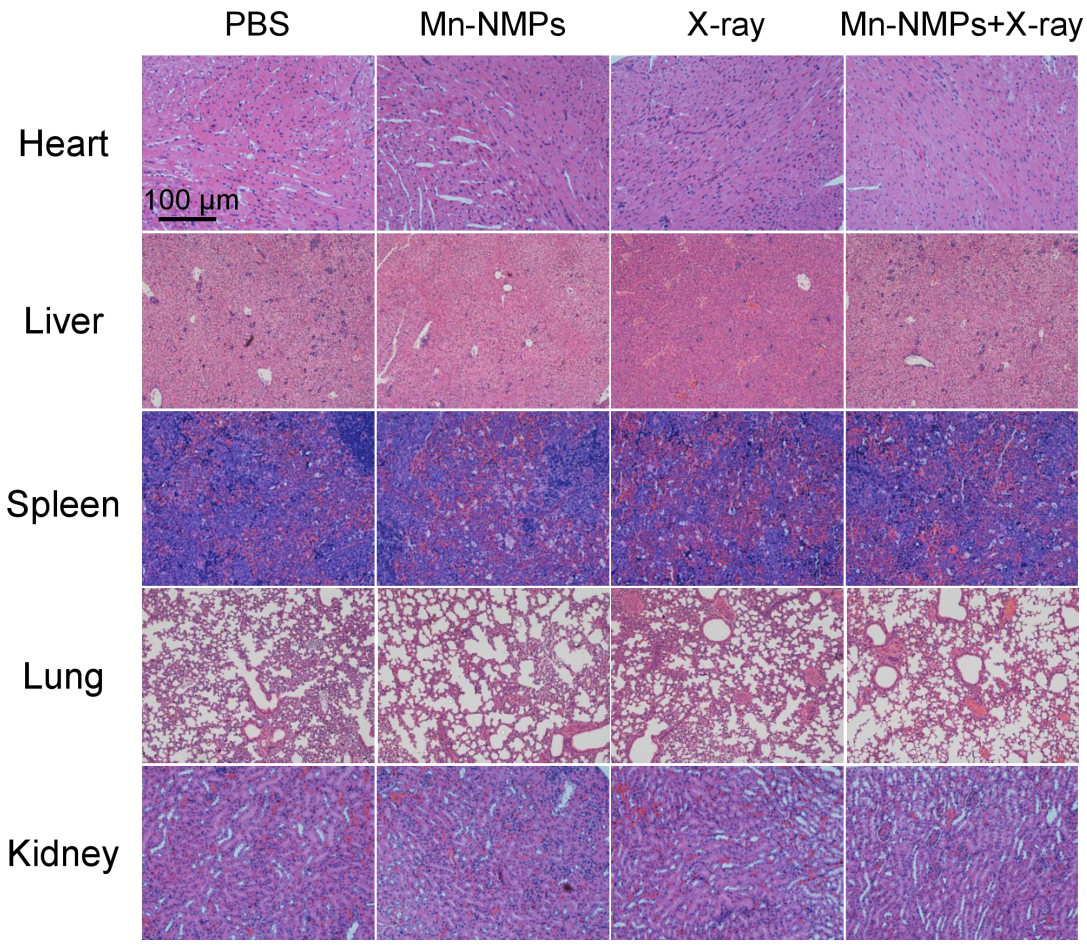

Figure S9. Related to **Figure 4.** H&E staining of mice hearts, livers, spleens, lungs and kidneys with different treatment.

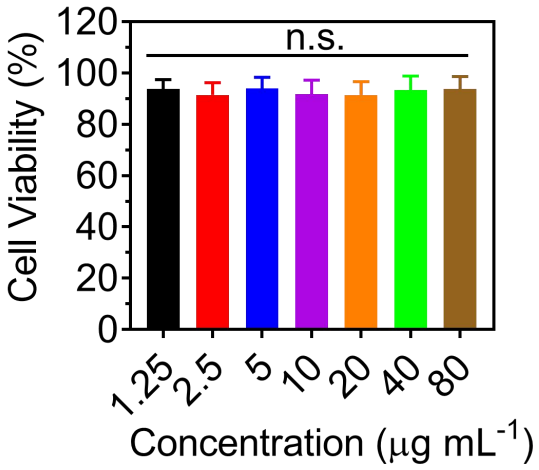

Figure S10. Related to **Figure 5.** Cell viability of RAW246.7 with the treatment of different concentration of Cu-NMPs.

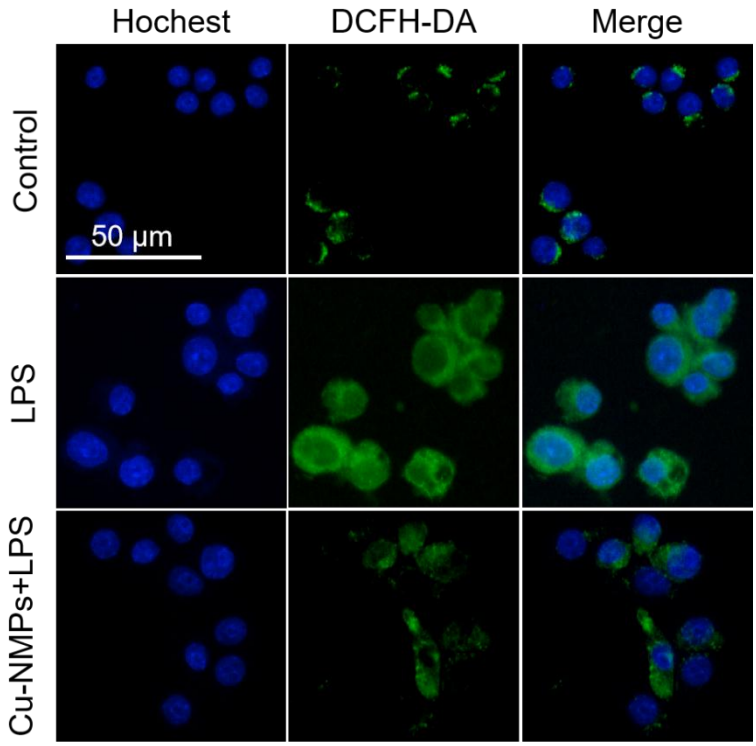

Figure S11. Related to **Figure 5.** Fluorescence microscopy images of ROS level in RAW264.7 with different treatments.

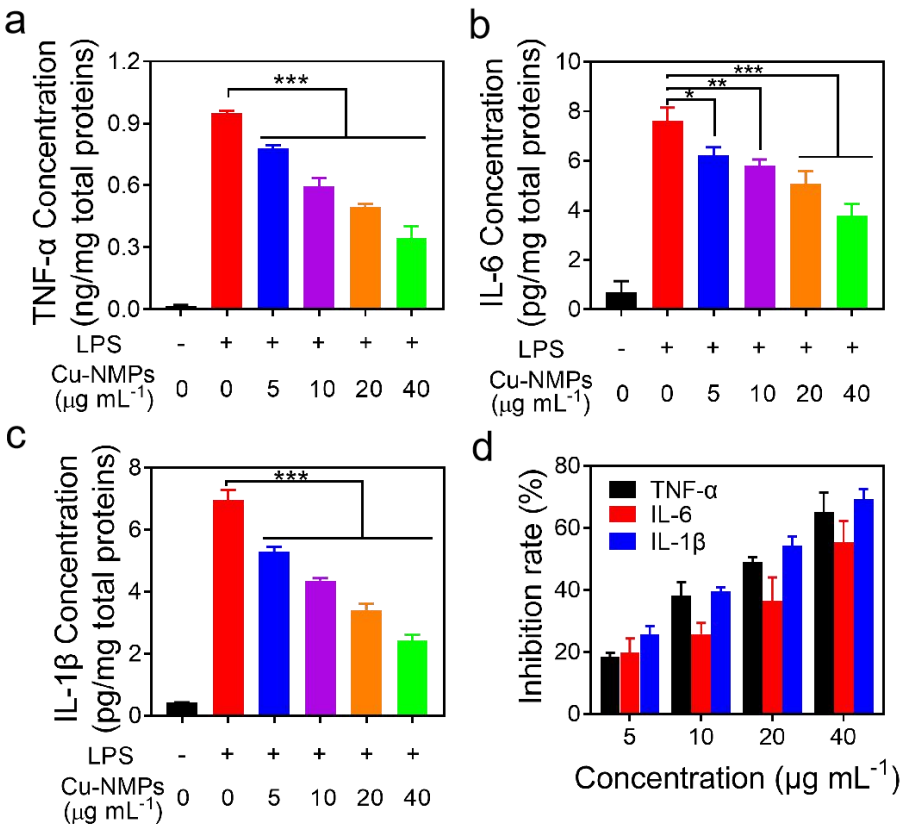

Figure S12. Related to **Figure 5.** The expression level of pro-inflammatory cytokines in LPS-stimulated RAW264.7 with different treatments. TNF-α (a), IL-6 (b) and IL-1β (c) expression levels in LPS-stimulated RAW264.7 with different concentrations of Cu-NMPs. (d) The inhibition rate of TNF-α, IL-6 and IL-1β expression with different concentrations of Cu-NMPs. Inhibition rate (%) = $[(C_p-C)/(C_p-C_n)] \times 100$ (C_n, C_p and C refer to the concentration of protein in negative control group (PBS treatment), positive control group (LPS treatment) and sample groups, respectively). Significance between each group was calculated using ANOVA with Tukey post hoc test. *P < 0.05, **P < 0.01, ***P < 0.001. Results are expressed as the mean ± S.D. of at least three independent experiments measured in triplicate.

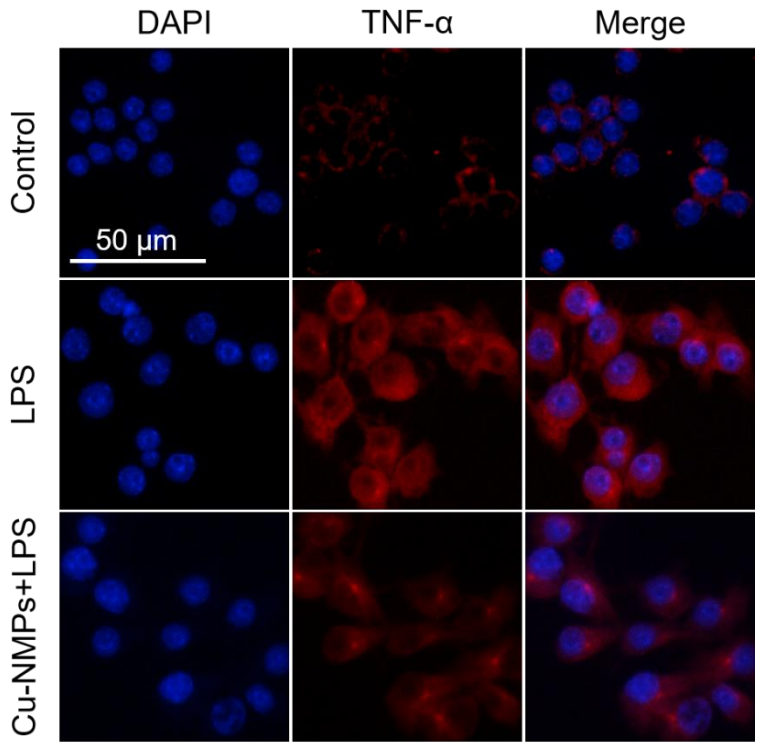

Figure S13. Related to **Figure 5.** Fluorescence microscopy images of TNF-α expression level in RAW264.7 with different treatments.

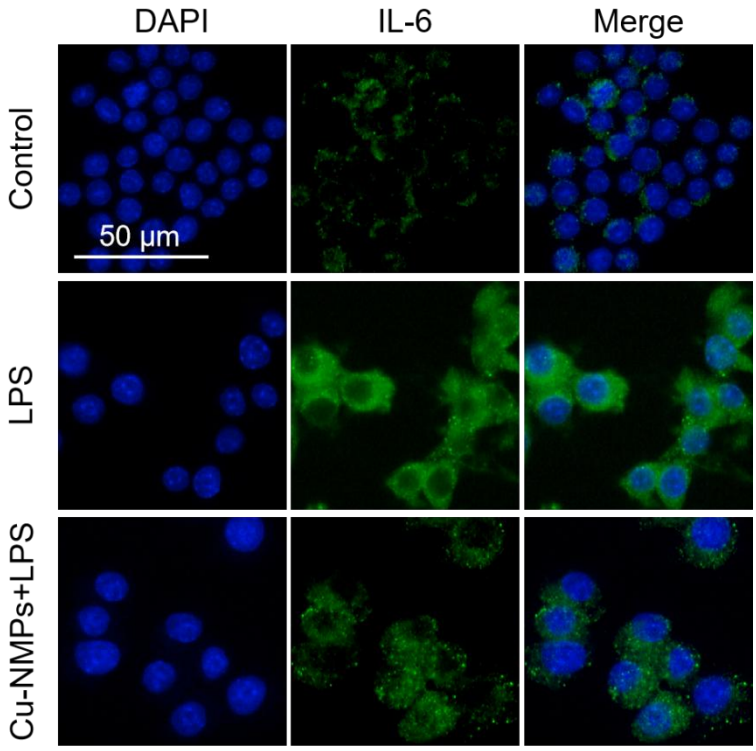

Figure S14. Related to **Figure 5.** Fluorescence microscopy images of IL-6 expression level in RAW264.7 with different treatments.

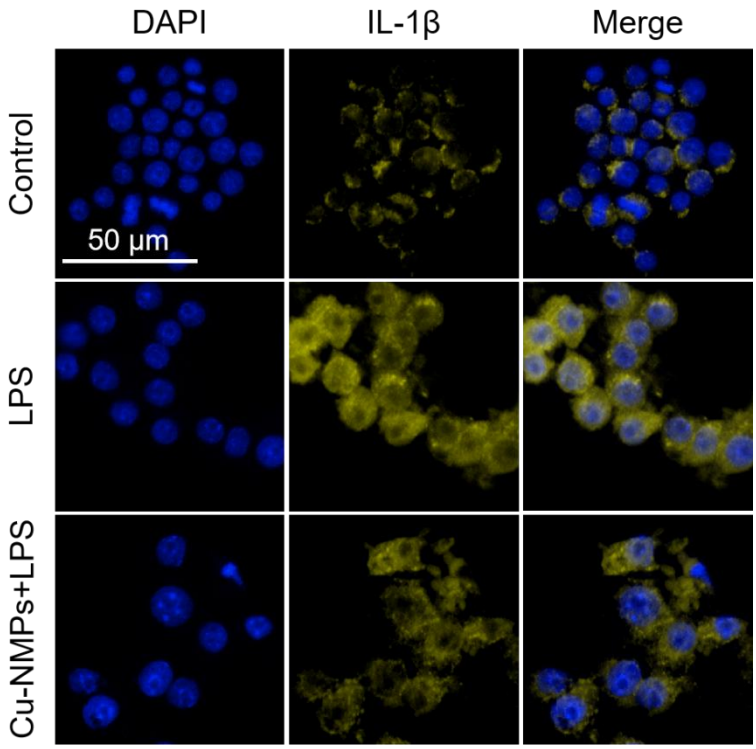

Figure S15. Related to **Figure 5.** Fluorescence microscopy images of IL-1β expression level in RAW264.7 with different treatments.

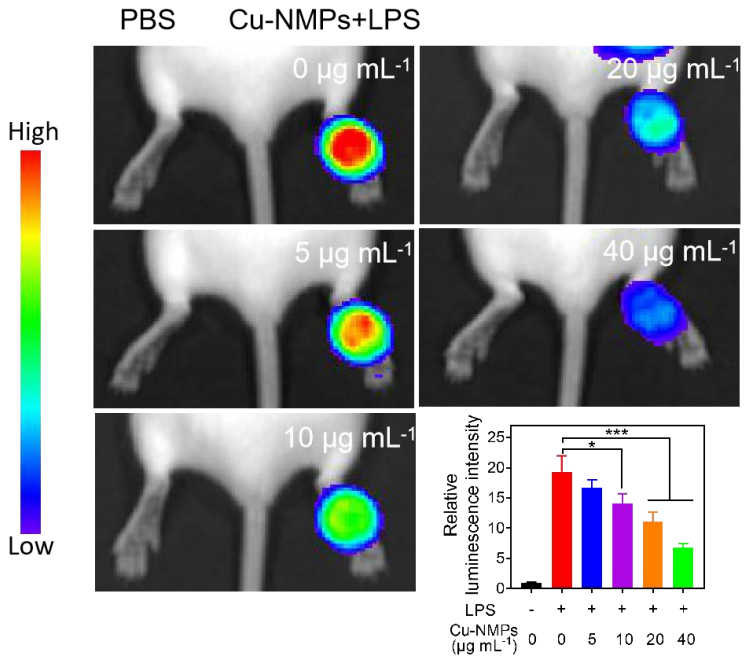

Figure S16. Related to **Figure 6.** *In vivo* bioluminescence images and corresponding luminescence intensities of ROS level in LPS-induced inflamed paws of mice with different concentrations of Cu-NMPs. Significance between each group was calculated using ANOVA with Tukey post hoc test. *P < 0.05, ***P < 0.001. Results are expressed as the mean ± S.D. of at least three independent experiments measured in triplicate.

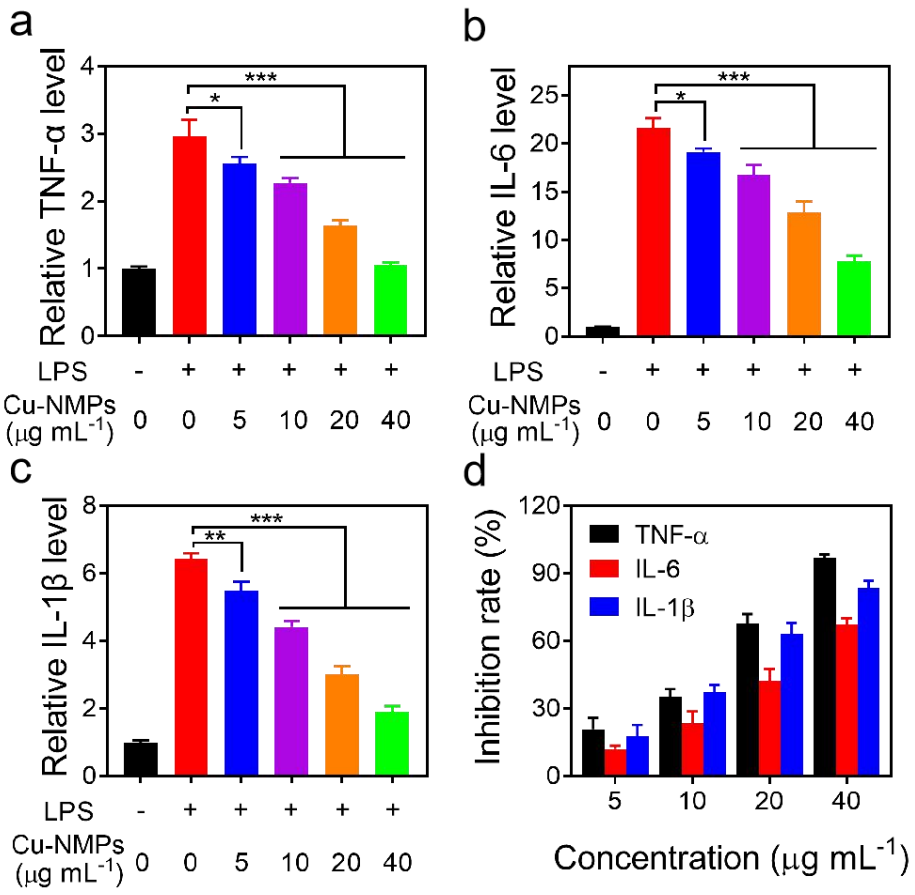

Figure S17. Related to **Figure 6.** The expression level of pro-inflammatory cytokines in LPS-induced inflamed paws with different treatment. TNF-α (a), IL-6 (b) and IL-1β (c) expression levels in LPS-induced inflamed paws of mice with different concentrations of Cu-NMPs. (d) The inhibition rate of TNF-α, IL-6 and IL-1β expression in LPS-induced inflamed paws of mice with different concentrations of Cu-NMPs. Inhibition rate (%) = $[(C_p-C)/(C_p-C_n)] \times 100$ (C_n, C_p and C refer to the concentration of protein in negative control group (PBS treatment), positive control group (LPS treatment) and sample groups, respectively). Significance between each group was calculated using ANOVA with Tukey post hoc test. *P < 0.05, **P < 0.01, ***P < 0.001. Results are expressed as the mean ± S.D. of at least three independent experiments measured in triplicate.

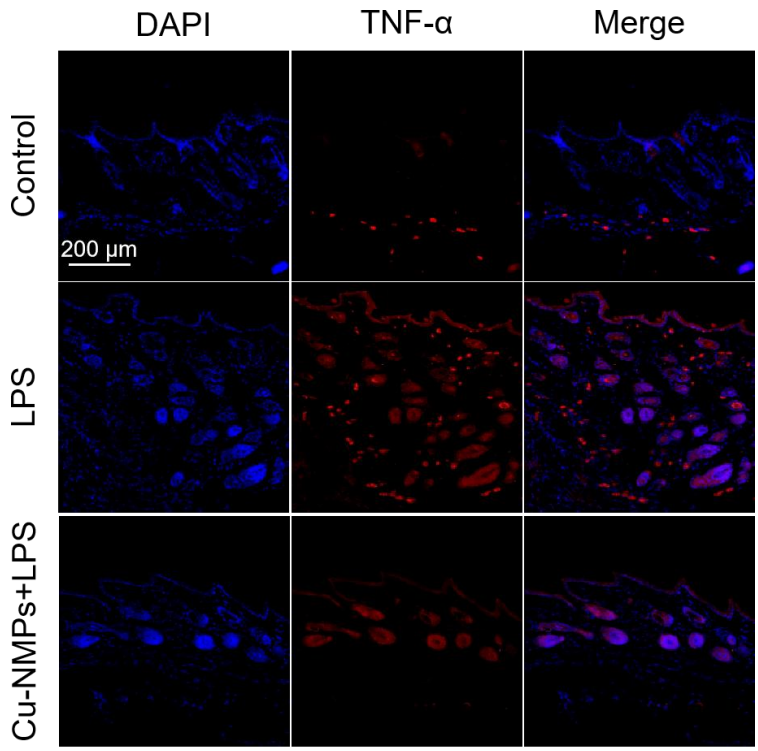

Figure S18. Related to **Figure 6.** Immunofluorescence staining of TNF-α expression in LPS-induced inflamed paws of mice with different treatment.

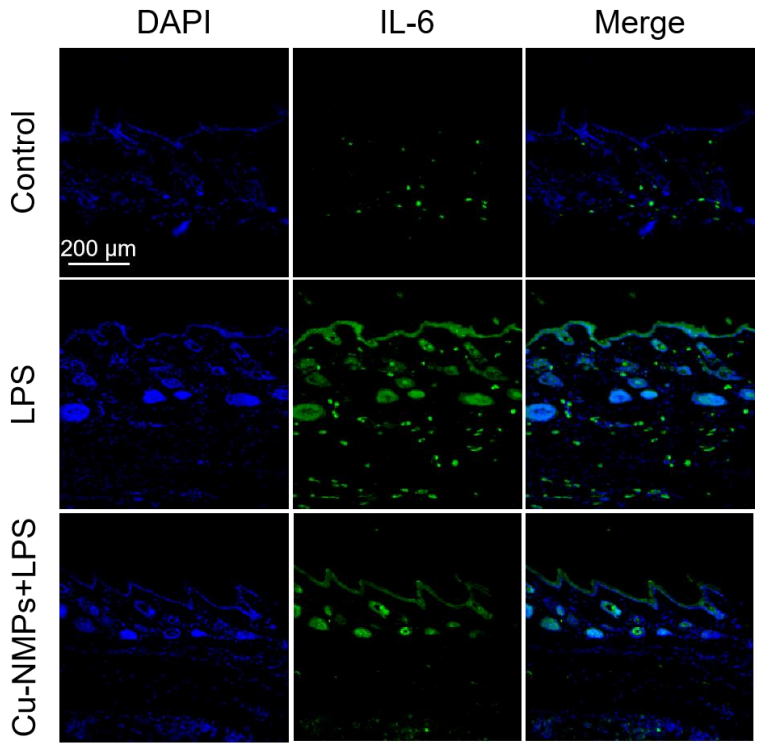

Figure S19. Related to **Figure 6.** Immunofluorescence staining of IL-6 expression in LPS-induced inflamed paws of mice with different treatment.

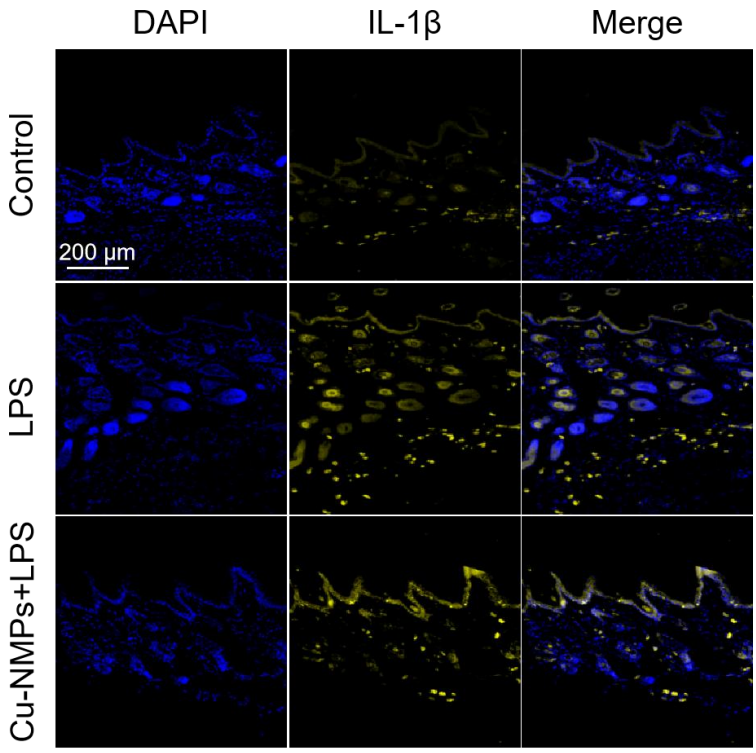

Figure S20. Related to **Figure 6.** Immunofluorescence staining of IL-1β expression in LPS-induced inflamed paws of mice with different treatment.

Supplemental Tables

Table S1. Related to **Figure 1.** The metal ions content in its corresponding M-NMPs.

Metal	Content (%)
Fe	4.0
Cu	5.1
Mn	4.2

Table S2. Related to **Figure 2.** The Michaelis-Menten constant (K_m) and maximum reaction rate (V_{max}) of Fe-NMPs and Cu-NMPs with TMB and H_2O_2 as the substrates for POD-like catalysis activity.

Catalyst	[E] (μg mL^{-1})	substrate	K_m (mM)	V_{max} (10^{-8} M s^{-1})
Fe-NMPs	10	TMB	0.46	2.49
Fe-NMPs	10	H_2O_2	394	4.11
Cu-NMPs	10	TMB	0.585	1.8
Cu-NMPs	10	H_2O_2	484	1.93